Transport in Porous Media **34:** 63–100, 1999.

B-41

Contributions to Theoretical/Experimental Developments in Shock Waves Propagation in Porous Media

S. SOREK[1,2], A. LEVY[2], G. BEN-DOR[2] and D. SMEULDERS[3]
[1] *J. Blaustein Institute for Desert Research, Water Resources Research Center, Sde Boker Campus, Israel*
[2] *Department of Mechanical Engineering, Pearlstone Center for Aeronautical Studies, Ben-Gurion University of the Negev, Beer Sheva, Israel*
[3] *Faculty of Applied Earth Sciences, Delft University of Technology, Delft, The Netherlands*

(Received: 22 June 1997; in final form: 30 October 1997)

Abstract. Macroscopic balance equations of mass, momentum and energy for compressible Newtonian fluids within a thermoelastic solid matrix are developed as the theoretical basis for wave motion in multiphase deformable porous media. This leads to the rigorous development of the extended Forchheimer terms accounting for the momentum exchange between the phases through the solid-fluid interfaces. An additional relation presenting the deviation (assumed of a lower order of magnitude) from the macroscopic momentum balance equation, is also presented. Nondimensional investigation of the phases' macroscopic balance equations, yield four evolution periods associated with different dominant balance equations which are obtained following an abrupt change in fluid's pressure and temperature. During the second evolution period, the inertial terms are dominant. As a result the momentum balance equations reduce to nonlinear wave equations. Various analytical solutions of these equations are described for the 1-D case. Comparison with literature and verification with shock tube experiments, serve as validation of the developed theory and the computer code.

A 1-D TVD-based numerical study of shock wave propagation in saturated porous media, is presented. A parametric investigation using the developed computer code is also given.

Key words: saturated and multiphase porous media, mass, momentum and energy balance equations, Forchheimer terms, Compaction waves, 1-D numerical simulation, shock tube experiments.

1. Introduction

The expected significance of research concerning the propagation of nonlinear waves in porous media is that it can serve as a tool in designing, for example porous plates covering, say, shelters or aircraft wings enabling the attenuation of the blast intensity. The analysis of changes produced in waves velocities may lead to the identification of different underground fluid pockets. Such modeling can also develop a methodology for cleaning groundwater from trapped contaminants which are localized at specific sites. It can explore the effect of shock waves sweeping over dust layers or sand dunes. Such modeling can also develop a methodology for pressure amplification when shock waves are discharged towards a collision at a focal point.

A porous material as defined by Gibson and Ashby [18] is a material 'made up of an interconnected network of solid strata or plates which forms the edges and faces of cells'. In general, porous materials can be divided into flexible or rigid. We use the term *rigid* in the loose relative sense which is common when applied to porous materials in general, and foams, in particular, that is the strain does not exceed a few percent. Unlike flexible porous materials which can undergo very large deformations (the strain can reach values larger than 0.9) even when moderate forces act on them, rigid porous materials do not exhibit usually large deformations. Many researchers have investigated experimentally the interaction of planar shock waves with flexible porous materials, e.g., Gelfand *et al.* [17], Gvozdeva *et al.* [21], Henderson *et al.* [24], Skews [46], Skews *et al.* [47] and Ben-Dor *et al.* [10]. Experimental investigation of the head-on collision of planar shock waves with rigid porous materials were reported by Sandusky and Liddiard [45] and Levy *et al.* [30]. In all the above-mentioned studies the pores of the porous material were air saturated. The interaction of planar shock waves with water saturated or unsaturated porous materials was reported by Zaretsky and Igra [53] for flexible polyurethane foams and van der Grinten *et al.* [20] for solid porous materials which were made by gluing together sand particles.

In recent years, the authors were involved in developing the theoretical basis and experimental verifications for wave motion in multiphase deformable porous media ([7–11, 26, 27, 29–35, 38, 48–52]). These were formulated in the form of macroscopic balance equations of mass, momentum and energy for compressible Newtonian fluids within a thermoelastic solid matrix.

In general, two type of approaches have been employed by researches for treating the above-mentioned interactions.

1.1. THE SINGLE PHASE APPROACH

The basic idea in the single phase approach is to replace the solid matrix $(\ )_s$, and the fluid $(\ )_f$, occupying the pores, by a single fictitious phase. This approach has been applied in two different ways. The first, known as the *bulk approach* is appropriate for both flexible and rigid porous materials. The second, known as the *pseudo-gas approach*, is appropriate to gas saturated weak flexible porous materials.

1.1.1. *The Bulk Approach*

In this approach, the porous material is assumed to be a single phase whose properties are derived from the properties of the individual phases comprising it. The Lagrangian governing equations describing the head-on collision of planar shock waves with flexible foams were developed by Mazor *et al.* [38]. Numerical simulations based on this model were conducted by Ben-Dor *et al.* [10]. Relatively good agreement was evident when the numerical predictions were compared to experimental results.

1.1.2. *The Pseudo-Gas Approach*

Gelfand *et al.* [17] proposed a pseudo-gas approach, in which the gaseous phase and the foam matrix are treated as a homogeneous pseudo-gas with new properties. As a result of this approach, the interaction problem is reduced to the refraction of a planar shock wave at a gaseous interface (that is the interface separating the pure gas and the pseudo gas). Consequently, the flow field can be calculated using gas dynamic relations with the boundary condition that the pressures and the velocities in the flow states in either side of the gas/foam interface are equal.

Gvozdeva and Faresov [22] adopted Gelfand *et al.*'s [17] pseudo-gas model and presented an analytical model for the calculation of various parameters in the flow field (for example, the compaction wave velocity, the compaction induced flow velocity, etc.).

A similar approach was adopted by Li and Ben-Dor [35]. However, their model was limited to analytical predictions of the flow field in the vicinity of the gas/foam interface immediately after the front edge of the foam was struck head-on by the planar shock wave.

1.2. THE MULTIPHASE APPROACH

In this approach, the porous medium is considered as a multiphase in which the various phases interact with each other. A detailed description of this approach was given by Baer and Nunziato [5]. A one-dimensional two-phase analysis of air as the fluid phase was presented by Baer [3] and Powers *et al.* [44]. In addition to numerical solutions, Baer [3], Powers *et al.* [44] and Levy *et al.* [31] also presented simplified analytical models for calculating the jump conditions across compaction waves in rigid porous materials.

Biot's [12] work on compression waves propagation was probably the first one to employ the fundamentals of porous media mechanics. A large number of papers have appeared in the literature following Biot's pioneering work. Among the recent ones are those by Smeulders *et al.* [48], Degrande and de Roeck [14] and Nigmatulin and Gubaidullin [41]. Basically these refer to microscopic representations of the phases' balance equations within the framework of the theory of mixtures. Most refer to linear waves which take place when momentum dissipation terms dominate. As an example, Attenborough [1] presents a theory dealing with the motion of sound waves through an ideal saturated porous matrix with parallel cylindrical pores. Using microscopic physical parameters, he extended this to account for randomly distributed pores. An extensive literature survey of similar approaches is given by Corapcioglu [13].

A series of shock tube experiments in which the interaction of weak planar shock waves with low density flexible foams was conducted by Skews [46]. Baer [4] presented an analytical model, based on the continuum mixture theory for describing the shock-foam (porous material) interaction phenomenon. His numerical simulations were found to agree quite well with Skews [46] experiments. For these experiments, better resolutions were obtained by Olim *et al.* [43] who considered the matrix as dust particles. As a result, the problem was replaced by the well known problem of calculating the relaxation zone in dusty shock waves (for details see Igra and Ben-Dor [26]). In the momentum interaction they replaced the classical expressions for the drag force by Darcy–Forchheimer forces. Olim *et al.* [43] noted correctly that this approach can be justified only for infinitely weak foams in which the internal stresses are negligibly small.

Macroscopic mass, momentum and energy balance equations for the fluid phase and the solid matrix were formulated on the basis of *representative elementary volume* (REV) concepts by Bear and Bachmat [6]. Based on these, Bear and Sorek [7] developed the dominant macroscopic forms of the mass and momentum balance equations following an abrupt pressure impact in saturated porous materials under isothermal conditions. It was shown that during a certain time period, due to the domination of momentum inertial terms, the fluid momentum balance equation conforms to nonlinear wave forms.

This initiated the establishment of the macroscopic theoretical basis for wave motion in multiphase deformable porous media.

Bear *et al.* [8] and Sorek *et al.* [49] elaborated on these for the case of thermoelastic porous media, describing the theoretical basis for obtaining displacement and shock waves, respectively. Following Sorek *et al.* [49], Levy *et al.* [32] introduced additional Forchheimer terms and obtained a variety of nonlinear wave equation forms. These together with the development of the evolving balance equations following an abrupt simultaneous change of the fluid temperature and pressure, are the major novel theoretical aspects when compared with Nikolaevskij [42].

Based on the findings of Powers *et al.* [44], these macroscopic equations were simplified by Levy *et al.* [31] who proposed analytical expressions for calculating the jump conditions across compaction waves in rigid porous materials. The predictions of the model developed by Levy *et al.* [31] were found to be better than those of Powers *et al.* [44] when they were compared to the experimental results of Sandusky and Liddiard [45].

Krylov *et al.* [27] presented a 1-D simple analytical solution of the macroscopic isothermal case. The wave equation was transformed to Euler's equation describing the motion of a 'new' fluid with properties related to the fluid which actually occupied the pores of the porous material. A similar analytical solution was presented by Sorek *et al.* [51] for the nonisothermal case. In that study they presented a method leading to generalized fluid density, pressure and temperature. Using their generalized properties Euler's equation was rewritten as the 1-D expression for the analytical solution of the fluid's equation of motion. To obtain this, the porosity, the matrix strain and temperature of the solid were developed as explicit functions of pressure.

The coupled changes between solute's mass balance equation and the 'new' fluid wave equation, were developed theoretically and solved analytically for a 1-D case by Sorek and Levy-Hevroni [50] and Sorek [52] for nondeformable and deformable, respectively, saturated porous media.

In the following we will present the development leading to the macroscopic nonlinear wave equations for a fluid in saturated deformable and thermoelastic porous media.

2. Phase Balance Equations

As a starting point for analyzing the motion of a phase, that is the spatial and temporal changes that it may undergo as a result of various excitations, Bear and Bachmat [6] describe the general form for a microscopic balance equation for an extensive quantity in a single phase continuum. The microscopic balance equations for each phase are then transformed by *averaging* rules, Bachmat and Bear [2] and Bear and Bachmat [6], into macroscopic equivalents using REV concepts.

2.1. MACROSCOPIC BALANCE EQUATIONS

In a saturated porous medium, a compressible Newtonian fluid and a thermoelastic solid matrix, the phases' macroscopic balance equations, neglecting their dispersive flux terms, read:

The fluid mass balance equation:

$$\frac{\partial}{\partial t}(\phi\bar{\rho}_{\mathrm{f}}^{\mathrm{f}}) = -\nabla\cdot(\phi\bar{\rho}_{\mathrm{f}}^{\mathrm{f}}\overline{\mathbf{V}_{\mathrm{f}}}^{\mathrm{f}}). \tag{1}$$

The solid mass balance equation:

$$\frac{\partial}{\partial t}[(1-\phi)\bar{\rho}_{\mathrm{s}}^{\mathrm{s}}] = -\nabla\cdot[(1-\phi)\bar{\rho}_{\mathrm{s}}^{\mathrm{s}}\overline{\mathbf{V}_{\mathrm{s}}}^{\mathrm{s}}], \tag{2}$$

where $\bar{e}_\alpha^\alpha$ denotes the average of an intensive variable e_α, over the α-phase ($\alpha \equiv \mathrm{f}, \mathrm{s}$) within the REV, ρ denotes the mass density of the phase, ϕ denotes the porosity and $\mathbf{V}$ denotes the mass weighted velocity of the phase.

The general form of the momentum balance equation for the α phase, assuming that the micoroscopic solid–fluid interface $\mathcal{S}_{\mathrm{fs}}$ is material to mass flux, reads

$$\begin{aligned}
&\frac{\partial}{\partial t}[\theta_\alpha(\bar{\rho}_\alpha^\alpha\overline{\mathbf{V}_\alpha}^\alpha + \overline{\mathbf{d}_\alpha^M}^\alpha)] \\
&\quad = -\nabla\cdot[\theta_\alpha(\bar{\rho}_\alpha^\alpha\overline{\mathbf{V}_\alpha}^\alpha\overline{\mathbf{V}_\alpha}^\alpha - \overline{\boldsymbol{\sigma}_\alpha}^\alpha + \overline{\mathbf{d}_\alpha^M}^\alpha\overline{\mathbf{V}_\alpha}^\alpha + \overline{(\rho_\alpha\overset{\circ}{\mathbf{V}}_\alpha)\overset{\circ}{\mathbf{V}}_\alpha}^\alpha)] + \\
&\qquad + \frac{1}{\mathcal{U}_0}\int_{\mathcal{S}_{\mathrm{fs}}}\boldsymbol{\sigma}_\alpha\cdot\boldsymbol{\xi}\,\mathrm{d}s + \theta_\alpha\overline{\rho_\alpha\mathbf{F}_\alpha}^\alpha,
\end{aligned} \tag{3}$$

in which θ_α denotes the volume fraction of the α phase, $\boldsymbol{\sigma}_\alpha$ denotes its stress tensor, $\mathbf{F}_\alpha$ denotes its body force vector, $\mathcal{U}_0$ denotes the REV volume, $\boldsymbol{\xi}$ denotes a unit vector perpendicular to the REV interface and $\overline{\mathbf{d}_\alpha^M}^\alpha$ ($\equiv \overline{\overset{\circ}{\rho}_\alpha\overset{\circ}{\mathbf{V}}_\alpha}^\alpha$) denotes the variations vector (within the volume of the α phase in REV) from the specific momentum of the α

phase. In obtaining the macroscopic momentum balance equations, we neglect $\overline{\mathbf{d}_\alpha^M}^\alpha$ (i.e., $\left|\bar{\rho}_\alpha^\alpha \overline{\mathbf{V}_\alpha}^\alpha\right| \gg \left|\overline{\mathbf{d}_\alpha^M}^\alpha\right|$), as well as the dispersive flux of momentum $(\overline{(\rho_\alpha \mathring{\mathbf{V}}_\alpha)\mathring{\mathbf{V}}_\alpha}^\alpha)$ compared with the advective one $(\bar{\rho}_\alpha^\alpha \overline{\mathbf{V}_\alpha}^\alpha \overline{\mathbf{V}_\alpha}^\alpha)$.

To evaluate the value of $\overline{\mathbf{d}_\alpha^M}^\alpha$, we need to solve separately the momentum balance equation of the *deviation terms*. Concerning the fluid, this reads

$$\frac{\partial}{\partial t}(\phi \overline{\mathbf{d}_\mathrm{f}^M}^\mathrm{f}) = -\nabla \cdot \left[\phi\left(\overline{\mathbf{d}_\mathrm{f}^M}^\mathrm{f} \mathring{\mathbf{V}}_\mathrm{f}^\mathrm{f} + \overline{(\rho_\mathrm{f}\, \mathring{\mathbf{V}}_\mathrm{f})\mathring{\mathbf{V}}_\mathrm{f}}^\mathrm{f}\right)\right]. \tag{4}$$

We note that the first RHS term in (4), represents an advective flux of this momentum balance equation. To solve for $\overline{\mathbf{d}_\alpha^M}^\alpha$ in (4), we need first to solve the macroscopic mass and momentum balance equations from which we will estimate $\overline{\mathbf{V}_\mathrm{f}}^\mathrm{f}$, the phase macroscopic velocity. Moreover, as an approximation of (4), we can assume that the second RHS term (the dispersive flux of the momentum) is negligible in comparison to the advective one.

Unlike Bear and Bachmat [6], for high fluid velocities and based on the microscopic momentum balance equation of the fluid at $\mathcal{S}_\mathrm{fs}$, the solid–fluid interface, we assume

$$\left|\left(\rho_{\mathrm{f}_j}\frac{\partial V_{\mathrm{f}_j}}{\partial t} - \frac{\partial \tau_{\mathrm{f}_{ij}}}{\partial x_i}\right)\xi_j\right| \ll \left|\left(\frac{\partial P}{\partial x_j} + \rho_\mathrm{f} g \frac{\partial Z}{\partial x_j} + \rho_\mathrm{f} V_{\mathrm{f}_j}\frac{\partial V_{\mathrm{f}_j}}{\partial x_i}\right)\xi_j\right| \tag{5}$$

in which $\tau_{f_{ij}}$ denotes the shear stress tensor of the Newtonian fluid, P denotes its pressure, $\mathbf{g}$ denotes the gravity acceleration vector, Z denotes the altitude parallel to $\mathbf{g}$. We then obtain,

The fluid momentum balance equation:

$$\begin{aligned}
\phi\bar{\rho}_\mathrm{f}^\mathrm{f}\frac{D_\mathrm{f}}{Dt}(\overline{\mathbf{V}_\mathrm{f}}^\mathrm{f}) \;=\;& -\phi\mathbf{T}_\mathrm{f}^*(\nabla\bar{P}^\mathrm{f} + \bar{\rho}_\mathrm{f}^\mathrm{f} g\nabla Z) - \frac{c_\mathrm{f}}{2\Delta_\mathrm{f}^2}\frac{\bar{\rho}_\mathrm{f}^\mathrm{f}}{\phi}\tilde{\mathbf{F}}\mathbf{q}_\mathrm{r}\mathbf{q}_\mathrm{r} + \\
& + \bar{\rho}_\mathrm{f}^\mathrm{f}(\mathbf{I} - \mathbf{T}_\mathrm{f}{}^*)(\nabla\mathbf{q}_\mathrm{r} + \phi\nabla\overline{\mathbf{V}_\mathrm{s}}^\mathrm{s})\cdot\overline{\mathbf{V}_\mathrm{s}}^\mathrm{s} + \\
& + (\bar{\mu}_\mathrm{f}^\mathrm{f} + \overline{\lambda''_\mathrm{f}}^\mathrm{f})[\nabla(\nabla\cdot\mathbf{q}_\mathrm{r} + \phi\nabla\cdot\overline{\mathbf{V}_\mathrm{s}}^\mathrm{s}) - (\nabla\cdot\overline{\mathbf{V}_\mathrm{f}}^\mathrm{f})\nabla\phi] + \\
& + \bar{\mu}_\mathrm{f}^\mathrm{f}\left[\nabla\cdot(\nabla\mathbf{q}_\mathrm{r} + \phi\nabla\overline{\mathbf{V}_\mathrm{s}}^\mathrm{s}) - \frac{c_\mathrm{f}}{\Delta_\mathrm{f}^2}\boldsymbol{\alpha}\mathbf{q}_\mathrm{r}\right],
\end{aligned} \tag{6}$$

where $\mathrm{D}_\alpha/\mathrm{D}t \equiv \partial/\partial t + \mathbf{V}_\alpha \cdot \nabla$ denotes the *material derivative*, which expresses the rate of change from the point of view of an observer traveling at the velocity $\mathbf{V}_\alpha$, $\bar{\mu}_\mathrm{f}^\mathrm{f}$ and $\overline{\lambda''_\mathrm{f}}^\mathrm{f}$ denote, respectively, the first and second fluid viscosities, c_f denotes a shape factor, $\boldsymbol{\alpha}$ denotes a tensor associated with the matrix directional cosines, Δ_f denotes the hydraulic radius of the pore spaces, $\mathbf{I}$ denotes a unit tensor, $\mathbf{q}_\mathrm{r}(\equiv \phi\bar{\mathbf{V}}_\mathrm{r})$ denotes the specific flux related to the relative velocity $\bar{\mathbf{V}}_\mathrm{r}(\equiv \overline{\mathbf{V}_\mathrm{f}}^\mathrm{f} - \overline{\mathbf{V}_\mathrm{s}}^\mathrm{s})$ and $\tilde{\mathbf{F}}$ denotes the third rank Forchheimer tensor.

Note that the Forchheimer term originated from a microscopic inertial term at the solid–fluid interface (see also Du Plessis and Masliyan [15] and Du Plessis *et al.* [16]). This is in contradiction to the assumption made by Hsu and Cheng [25], Nield [39, 40], and Olim *et al.* [43] who refer to it as a drag force.

The porous medium momentum balance equation

By summing the macroscopic momentum balance equations for the fluid and for the thermoelastic solid phases, the rate of momentum exchange across the solid–fluid interface is eliminated and we obtain the momentum balance equation for the porous medium as a whole in the form

$$\begin{aligned}\bar{\rho}_\mathrm{b}\frac{\mathrm{D_s}}{\mathrm{D}t}(\overline{\mathbf{V}_\mathrm{s}}^\mathrm{s}) + \phi\bar{\rho}_\mathrm{f}^\mathrm{f}\frac{\mathrm{D_r}}{\mathrm{D}t}(\bar{\mathbf{V}}_\mathrm{r}) &= -\phi\bar{\rho}_\mathrm{f}^\mathrm{f}(\bar{\mathbf{V}}_\mathrm{r}\nabla\cdot\overline{\mathbf{V}_\mathrm{s}}^\mathrm{s} + \overline{\mathbf{V}_\mathrm{s}}^\mathrm{s}\nabla\cdot\mathbf{V}_\mathrm{r}) + \nabla\cdot\bar{\boldsymbol{\sigma}}_\mathrm{t} + \\ &\quad + \bar{\rho}_\mathrm{b}g\nabla Z + \frac{1}{\mathcal{U}_0}\int_{\mathcal{S}_\mathrm{fs}}(\boldsymbol{\sigma}_\mathrm{f} - \boldsymbol{\sigma}_\mathrm{s})\cdot\boldsymbol{\xi}_\mathrm{f}\,\mathrm{d}S, \end{aligned}\tag{7}$$

where $\bar{\rho}_\mathrm{b}$ denotes the *bulk density*, given by

$$\bar{\rho}_\mathrm{b} \equiv \phi\bar{\rho}_\mathrm{f}^\mathrm{f} + (1-\phi)\bar{\rho}_\mathrm{s}^\mathrm{s}, \tag{8}$$

the *total bulk stress* $\bar{\boldsymbol{\sigma}}_\mathrm{t}$ is given by

$$\bar{\boldsymbol{\sigma}}_\mathrm{t} \equiv \phi\bar{\boldsymbol{\sigma}}_\mathrm{f}^\mathrm{f} + (1-\phi)\bar{\boldsymbol{\sigma}}_\mathrm{s}^\mathrm{s} = \bar{\boldsymbol{\sigma}}'_\mathrm{s} + \bar{\boldsymbol{\sigma}}_\mathrm{f}^\mathrm{f}, \tag{9}$$

in which $\bar{\boldsymbol{\sigma}}'_\mathrm{s}$ denotes the effective stress tensor for the thermoelastic solid matrix in which its constitutive relation is assumed to be similar to its microscopic one,

$$\bar{\boldsymbol{\sigma}}'_\mathrm{s} = 2\overline{\mu'_\mathrm{s}}^\mathrm{s}\boldsymbol{\varepsilon}_{sk} + [\overline{\lambda''_\mathrm{s}}^\mathrm{s}\varepsilon_{sk} - \bar{\eta}(\overline{T_\mathrm{s}}^\mathrm{s} - \overline{T_{\mathrm{s}_0}}^\mathrm{s})]\mathbf{I} \tag{10}$$

$\overline{T_\alpha}^\alpha$ denotes the α-phase temperature, $\overline{\mu'_\mathrm{s}}^\mathrm{s}$, $\overline{\lambda''_\mathrm{s}}^\mathrm{s}$ and $\bar{\eta}$ denote the Lame's constants for a thermoelastic solid matrix, $\boldsymbol{\varepsilon}_{sk}$ and ε_{sk} denote, respectively, its strain tensor and volumetric strain associated with $\mathbf{w}_\mathrm{s}$, its displacement vector, and defined by

$$\boldsymbol{\varepsilon}_{sk} = \tfrac{1}{2}[\nabla\mathbf{w}_\mathrm{s} + (\nabla\mathbf{w}_\mathrm{s})^T]; \quad \varepsilon_{sk} = \nabla\cdot\mathbf{w}_\mathrm{s}. \tag{11}$$

In writing the macroscopic energy balance equations for the fluid and the solid phases, we assume linear thermodynamics, omit external energy sources and the energy associated with the fluid shear tensor $\bar{\boldsymbol{\tau}}_\mathrm{f}^\mathrm{f}$ (viscous dissipation) is assumed to be negligible. We thus obtain:

The fluid energy balance equation:

$$\begin{aligned}&\frac{\partial}{\partial t}\left\{\phi\bar{\rho}_\mathrm{f}^\mathrm{f}\left[C_\mathrm{f}\overline{T_\mathrm{f}}^\mathrm{f} + \frac{(\overline{V_\mathrm{f}}^\mathrm{f})^2}{2}\right]\right\} \\ &= \mathbf{T}_\mathrm{s}^*\bar{P}^\mathrm{f}\overline{\mathbf{V}_\mathrm{s}}^\mathrm{s}\cdot\nabla\phi - \mathbf{T}_\mathrm{f}^*\nabla\cdot(\phi\bar{P}^\mathrm{f}\overline{\mathbf{V}_\mathrm{f}}^\mathrm{f}) - \alpha^{*\mathrm{H}}(\overline{T_\mathrm{f}}^\mathrm{f} - \overline{T_\mathrm{s}}^\mathrm{s}) + \\ &\quad + \overline{\mathbf{V}_\mathrm{s}}^\mathrm{s}\cdot\left[\frac{c_\mathrm{f}}{2\Delta_\mathrm{f}^2}\frac{\bar{\rho}_\mathrm{f}^\mathrm{f}}{\phi}\tilde{\mathbf{F}}\,\mathbf{q}_\mathrm{r}\mathbf{q}_\mathrm{r} + \bar{\rho}_\mathrm{f}^\mathrm{f}(\mathbf{I} - \mathbf{T}_\mathrm{f}^*)(\nabla\mathbf{q}_\mathrm{r} + \phi\nabla\overline{\mathbf{V}_\mathrm{s}}^\mathrm{s})\cdot\overline{\mathbf{V}_\mathrm{s}}^\mathrm{s}\right] - \end{aligned}$$

$$
- \nabla \cdot \left\{ \phi \bar{\rho}_f^f \left[C_f \overline{T_f}^f + \frac{(\overline{V_f}^f)^2}{2} \right] \overline{\mathbf{V}_f}^f \right\} +
$$
$$
+ \nabla \cdot [\phi \mathbf{D}^{*H} \boldsymbol{\nabla} (C_f \bar{\rho}_f^f \overline{T_f}^f) + \phi \bar{\lambda}_f^f \boldsymbol{\nabla} \overline{T_f}^f], \tag{12}
$$

where C_α denotes the constant specific heat at constant volume for the fluid phase ($\alpha \equiv f$) or at constant strain for the solid matrix ($\alpha \equiv$ s), $\overline{\lambda_\alpha}^\alpha$ denotes the thermal conductivity for the α-phase, α^{*H} denotes the heat transfer coefficient and $\mathbf{D}^{*H}$ denotes the dispersive heat tensor for the fluid.

The solid energy balance equation:

$$
\frac{\partial}{\partial t} \left\{ (1-\phi) \bar{\rho}_s^s \left[C_f \overline{T_s}^s + \frac{(\overline{V_s}^s)^2}{2} \right] \right\}
$$
$$
= -\alpha^{*H} (\overline{T_s}^s - \overline{T_f}^f) - \mathbf{T}_s^* \bar{P}^f \overline{\mathbf{V}_s}^s \cdot \boldsymbol{\nabla} \phi + \mathbf{T}_s^* \nabla \cdot [(1-\phi) \bar{P}^f \overline{\mathbf{V}_s}^s] - \nabla \cdot (\boldsymbol{\sigma}'_s \overline{\mathbf{V}_s}^s) -
$$
$$
- \overline{\mathbf{V}_s}^s \cdot \left[\frac{c_f}{2\Delta_f^2} \frac{\bar{\rho}_f^f}{\phi} \tilde{\mathbf{F}} \mathbf{q}_r \mathbf{q}_r + \bar{\rho}_f^f (\mathbf{I} - \mathbf{T}_f{}^*)(\boldsymbol{\nabla} \mathbf{q}_r + \phi \boldsymbol{\nabla} \overline{\mathbf{V}_s}^s) \cdot \overline{\mathbf{V}_s}^s \right] -
$$
$$
- \boldsymbol{\nabla} \cdot \left\{ (1-\phi) \bar{\rho}_s^s \left[C_s \overline{T_s}^s + \frac{(\overline{V_s}^s)^2}{2} \right] \overline{\mathbf{V}_s}^s - (1-\phi) \overline{\lambda_s}^s \boldsymbol{\nabla} \overline{T_s}^s \right\}. \tag{13}
$$

The set of balance equations (1), (2), (6), (7), (12) and (13) together with the definitions (8)–(11) can be solved for the macroscopic flow properties, given appropriate values for the various expressions representing the effects of small-scale features on the averaged large-scale flow. From hereafter we will refer to the macroscopic equations only and, accordingly, the $\overline{()}^\alpha$ designator will be omitted.

3. Dominant Forms of the Balance Equations Evolving After Abrupt Simultaneous Changes in Fluid Pressure and Temperature

In what follows we will describe the form of the dominant balance equations in a saturated porous media, obtained after abrupt simultaneous changes (e.g., in a well) in fluid pressure and temperature. Our objective is to analyze the order of magnitude of the flux terms appearing in the obtained macroscopic balance equations in order to eliminate nondominating ones. To achieve this goal, a dimensional analysis is carried out in which all the terms are compared with those associated with the rate of fluid pressure and temperature changes. In doing so, we follow Bear and Sorek [7], Sorek *et al.* [49] and Levy *et al.* [32]. Similar investigation can also be found in Sorek [52] in the case of abrupt change in pressure together with the problem of solute transport.

3.1. PERIOD OF UNIFORM DISTRIBUTIONS OF PRESSURE, STRESS AND TEMPERATURE

At the instant of abrupt change in the fluid's pressure and temperature, the nondimensional factors associated with these rates are of order one while all others are much smaller than one. This yields an approximate fluid mass balance equation in the form,

$$\left(\beta_{\mathrm{P}}\frac{\partial P}{\partial t}+\beta_{\mathrm{T}}\frac{\partial T_{\mathrm{f}}}{\partial t}\right)+V_{\mathrm{f}_j}\left(\beta_{\mathrm{P}}\frac{\partial P}{\partial x_j}+\beta_{\mathrm{T}}\frac{\partial T_{\mathrm{f}}}{\partial x_j}\right)=0 \tag{14}$$

for a compressible fluid ($\rho_{\mathrm{f}}=\rho_{\mathrm{f}}(P,T_{\mathrm{f}})$), denoting β_{P} and β_{T} as its pressure and temperature compressibilities, respectively. The solid matrix is deformable ($\phi=\phi(P)$) and assuming $|\partial\phi/\partial t|\gg|\mathbf{V}_{\mathrm{s}}\cdot\nabla\phi|$:

The fluid's momentum balance equation becomes

$$\phi T^*_{\mathrm{f}_{ij}}\frac{\partial P}{\partial x_j}=0. \tag{15}$$

The porous media momentum balance equation reads

$$\nabla\boldsymbol{\sigma}'_{\mathrm{s}}=(1-\phi)\rho_{\mathrm{s}}\,g\nabla Z. \tag{16}$$

The fluid energy balance equation is given by

$$|\mathbf{V}_{\mathrm{f}}+\mathbf{V}_{\mathrm{s}}|\nabla T_{\mathrm{f}}\cdot\nabla T_{\mathrm{f}}=0. \tag{17}$$

From (15) and (17) we note that P and T_{f} have constant distributions. Thus, this together with (14) yields

$$\beta_{\mathrm{P}}\frac{\partial P}{\partial t}=-\beta_{\mathrm{T}}\frac{\partial T_{\mathrm{f}}}{\partial t}. \tag{18}$$

Note that in view of (14) and (18), although the fluid is considered compressible, during this first time period it behaves as if it was incompressible, i.e.,

$$\rho_{\mathrm{f}}=\text{const.}\qquad\text{at}\quad t=0+. \tag{19}$$

The solid energy balance equation becomes

$$(1-\phi)\rho_{\mathrm{s}}C_{\mathrm{s}}\frac{\mathrm{D_s}T_{\mathrm{s}}}{\mathrm{D}t}=0, \tag{20}$$

hence, T_{s} remains constant along characteristic curves defined by

$$\frac{\mathrm{D_s}\mathbf{x}_{\mathrm{s}}}{\mathrm{D}t}=\mathbf{V}_{\mathrm{s}}, \tag{21}$$

where $\mathbf{x}_{\mathrm{s}}$ denotes the position vector along the characteristic path. The pressure and the fluid temperature impulse propagate without spatial attenuation over a characteristic, $()_c$, distance L_c^{P} defined by

$$L_c^{\mathrm{P}}\cong\mathrm{O}\left(\frac{t_c^{\mathrm{P}}}{\rho_{\mathrm{f}}\,\beta_{\mathrm{P}}\,V_c^{\mathrm{f}}}\right). \tag{22}$$

Hence, with the increase in time ($t = 0+$) at the onset of the fluid's pressure and temperature, throughout the L_c^{P} distance the fluid density will remain constant. This constitutes a linear ratio between the change of the fluid's pressure and temperature, both of which are uniformly distributed in space. The effective matrix stress is vertically uniformly distributed and constant elsewhere and its temperature and rate of change are related to its velocity.

3.2. PERIOD OF NONLINEAR WAVE PROPAGATION

After the first time period, it was concluded (Levy *et al.* [32]) that the fluid and the solid mass balance equations, remain in the form of (1) and (2), respectively.

During this time period, the fluid momentum balance equation conforms to

$$\phi\rho_{\mathrm{f}}\frac{\mathrm{D_f}}{\mathrm{D}t}(V_{\mathrm{f}_i}) + \phi T^*_{\mathrm{f}_{ij}}\left(\frac{\partial P}{\partial x_j} + \rho_{\mathrm{f}}\,g\frac{\partial Z}{\partial x_j}\right) + \frac{c_{\mathrm{f}}}{2\Delta_{\mathrm{f}}^2}\tilde{F}_{ijk}\,\phi\rho_{\mathrm{f}}V_{\mathrm{r}_j}V_{\mathrm{r}_k} = 0. \tag{23}$$

We subtract the fluid momentum balance equation from the porous medium momentum balance equation and assume that $|(1-\phi)\,\rho_{\mathrm{s}}| \gg |\phi\rho_{\mathrm{f}}(T_{\mathrm{s}}^* - T_{\mathrm{f}}^*)|$.

The obtained solid momentum balance equation, reads

$$(1-\phi)\rho_{\mathrm{s}}\frac{\mathrm{D_s}}{\mathrm{D}t}(V_{\mathrm{s}_i}) + (1-\phi)\left(T^*_{\mathrm{s}_{ij}}\frac{\partial P}{\partial x_j} + \rho_{\mathrm{s}}\,g\frac{\partial Z}{\partial x_i}\right) - \\ - \frac{\partial\sigma'_{\mathrm{s}_{ij}}}{\partial x_j} - \frac{c_{\mathrm{f}}}{2\Delta_{\mathrm{f}}^2}\tilde{F}_{ijk}\,\phi\rho_{\mathrm{f}}V_{\mathrm{r}_j}V_{\mathrm{r}_k} = 0. \tag{24}$$

The approximate energy balance equations conform to:

The fluid energy balance equation

$$\phi\rho_{\mathrm{f}}\left[C_{\mathrm{f}}\frac{\mathrm{D_f}}{\mathrm{D}t}(T_{\mathrm{f}}) + V_{\mathrm{f}_i}\frac{\mathrm{D_f}}{\mathrm{D}t}(V_{\mathrm{f}_i})\right] + T^*_{\mathrm{f}_{ij}}\left[\frac{\partial}{\partial x_i}(\phi P V_{\mathrm{f}_j}) - P\,V_{\mathrm{s}_j}\frac{\partial\phi}{\partial x_i}\right] + \\ + \frac{c_{\mathrm{f}}}{2\Delta_{\mathrm{f}}^2}\tilde{F}_{ijk}\,\phi\rho_{\mathrm{f}}V_{\mathrm{r}_j}V_{\mathrm{r}_k}V_{\mathrm{s}_i} = 0. \tag{25}$$

The solid energy balance equation

$$(1-\phi)\rho_{\mathrm{s}}\left[C_{\mathrm{s}}\frac{\mathrm{D_s}}{\mathrm{D}t}(T_{\mathrm{s}}) + V_{\mathrm{s}_j}\frac{\mathrm{D_s}}{\mathrm{D}t}(V_{\mathrm{s}_j})\right] + \\ + T^*_{\mathrm{s}_{ij}}\left[\frac{\partial}{\partial x_i}(1-\phi)PV_{\mathrm{s}_j} + P\,V_{\mathrm{s}_j}\frac{\partial\phi}{\partial x_i}\right] - \\ - \frac{\partial\sigma'_{\mathrm{s}_{ij}}}{\partial x_i}V_{\mathrm{s}_j} - \frac{c_{\mathrm{f}}}{2\Delta_{\mathrm{f}}^2}\tilde{F}_{ijk}\,\phi\rho_{\mathrm{f}}V_{\mathrm{r}_i}V_{\mathrm{r}_k}V_{\mathrm{s}_j} = 0. \tag{26}$$

On the basis of nondimensional scalars of the same order we note that the time span during which (23) to (26) are valid is given by

$$t_c^{\mathrm{P}} \cong \mathrm{O}\left(\frac{\beta_{\mathrm{P}}\,P_c\,V_c^{\mathrm{f}}}{g}\right). \tag{27}$$

During this period of evolution, inertial terms dominate and we note the emergence of nonlinear wave equations.

Actually, two more evolution stages are reported in Bear and Sorek [7] and Levy *et al.* [32]. During the third time period, the dissipative effects in the balance equations arise and become of the same order of magnitude as the inertial terms. During the fourth time period, the dissipative terms are dominating over the inertial ones. The various forms of the dominant balance equations during the third and fourth time periods are beyond the scope of this manuscript.

4. Analytical Solutions

4.1. ACROSS STRONG COMPACTION WAVES IN GAS SATURATED RIGID POROUS MEDIA

Based on experimental results and some additional simplifying assumptions, we show that the general macroscopic equations governing the flow field which is developed in a gas saturated rigid porous medium domain can be simplified to a form which enabled us to develop two analytical models for calculating the jump conditions across strong compaction waves.

Predictions obtained by these two simplified analytical models were compared to the experimental results of Sandusky and Liddiard [45] and to predictions of the model proposed by Powers *et al.* [44]. Fairly good to excellent agreements are evident.

In view of (1)–(13), we can write the *1-D mass, momentum and energy balance equations of the porous medium as a whole*. This we do by combining the fluid and solid balance equations, for each of the balance equations, noting that for the 1-D case $T_{\mathrm{f}}^{*} = T_{\mathrm{s}}^{*} = 1$. Dimensional analysis of these combined balance equations showed that the gaseous-phase terms were negligible in comparison to the solid-phase terms. Thus, the *1-D porous medium balance equations of mass, momentum and energy* could be approximated by those of the solid-phase ones. These, upon dropping the s subscript (e.g., $\theta \equiv \theta_{\mathrm{s}} = 1 - \phi$), read respectively

$$\frac{\partial}{\partial t}(\theta\rho) + \frac{\partial}{\partial x}(\theta\rho V) = 0, \tag{28}$$

$$\frac{\partial}{\partial t}(\theta\rho V) + \frac{\partial}{\partial x}(\theta\rho V^2 + \theta\sigma) = 0, \tag{29}$$

$$\frac{\partial}{\partial t}\left[\theta\rho\left(\mathcal{I} + \frac{V^2}{2}\right)\right] + \frac{\partial}{\partial x}\left[\theta\rho V\left(\mathcal{I} + \frac{V^2}{2} + \frac{\sigma}{\rho}\right)\right] = 0. \tag{30}$$

Based on findings of Baer [3] and Powers *et al.* [44] that the velocity of compaction waves is almost constant, one can further reduce (28)–(30) by applying the well known Galilean transformation (Ben-Dor [9]), i.e.,

$$\frac{\mathrm{d}}{\mathrm{d}\xi}(\theta\rho u) = 0, \tag{31}$$

$$\frac{\mathrm{d}}{\mathrm{d}\xi}(\theta\rho u^2 + \theta\sigma) = 0, \tag{32}$$

$$\frac{\mathrm{d}}{\mathrm{d}\xi}\left(\mathcal{I} + \frac{u^2}{2} + \frac{\sigma}{\rho}\right) = 0, \tag{33}$$

where $u \equiv V - \mathcal{D}$, $\xi \equiv x - \mathcal{D}t$ and $\mathcal{D}$ denotes the constant velocity of the compaction wave.

The above set (31)–(33), consists of three equations and five (ϕ, ρ, u, $\sigma, \mathcal{I}$) unknowns. Following Powers *et al.* [44], we add the *caloric equation for the solid phase*

$$\mathcal{I} + \frac{\sigma}{\rho} = \frac{\gamma}{(\gamma - 1)} \frac{\sigma + \mathcal{S}}{\rho}, \tag{34}$$

where γ and $\mathcal{S}$ are parameters that define Tait's equation of state. The value of γ is chosen to match the Hugoniot data. It is analogous to the specific heat ratio for equation of state of an ideal gas, $\mathcal{S}$ is the non-ideal solid parameter. When $\mathcal{S} = 0$, the equation of state is referred to as being ideal. An additional equation can be based on empirical relations (see, for example, the *compaction equation* in Powers *et al.* [44]). However, the parameters of this may need to be correlated with each separate experiment. Instead, we will prescribe one of the unknowns.

In what follows, we describe two simplified models. In the first, we assume that the solid phase density remains constant while in the second, post compaction wave porosity ϕ, is close to zero. The relations, as obtained from these two models, are presented in terms of $X_{21} \equiv X_2/X_1$ where X denotes a property of the solid phase (e.g., θ, σ, u, etc.), and the indices 1 and 2 denote location ahead and behind the compaction wave, respectively.

4.1.1. *Model I: Post Compaction Wave for Small Porosity Values*

It can be assumed that the solid phase starts to be compressed only when its volume fraction θ_2 approaches unity. Hence, when θ_2 is sufficiently smaller than unity, the solid phase can be assumed to be incompressible ($\rho_2 = \rho_1 \equiv \rho$). Under these assumptions (31)–(33), together with (34), can be integrated to read

$$\theta_1\mathcal{D} = \theta_2(\mathcal{D} - u), \tag{35}$$

$$\theta_1\rho\mathcal{D}^2 + \theta_1\sigma_1 = \theta_2\rho(\mathcal{D} - u)^2 + \theta_2\sigma_2, \tag{36}$$

$$\frac{\gamma}{(\gamma - 1)}\frac{\sigma_1 + \mathcal{S}}{\rho} + \frac{\mathcal{D}^2}{2} = \frac{\gamma}{(\gamma - 1)}\frac{\sigma_2 + \mathcal{S}}{\rho} + \frac{(\mathcal{D} - u)^2}{2}, \tag{37}$$

(35)–(37) can be combined to

$$\sigma_{21} = \frac{\Lambda + 1/\theta_{21}}{\Lambda + \theta_{21}}, \tag{38}$$

where

$$\Lambda \equiv \frac{1+\gamma}{1-\gamma}. \tag{39}$$

Note the similarity between (38) and the well known Rankine–Hugoniot equation which relates the pressure to density ratios across shock waves in gases (e.g., Glass and Hall [19], p. 66). When rewriting (38) as a function of θ_{21}, it becomes evident that $\theta_{21} \to -\Lambda$ when $\sigma_{21} \to \infty$ and that $\theta_{21} = 1$ when $\sigma_{21} = 1$.

In order to relate the normal stress ratio across the compaction wave to the compaction wave, $M_s(\equiv \mathcal{D}/c_1)$, Mach number, we use Powers *et al.* [44] to express c_1 the sound speed in the solid ($c = \pm\sqrt{\partial\sigma/\partial\rho}$), ahead of the compaction wave. Combining (35), (36) and (38) yields

$$M_s = \left[\frac{(\Lambda-1)\theta_{21}}{\gamma(1+\bar{\mathcal{S}})(\Lambda+\theta_{21})}\right]^{1/2}, \tag{40}$$

where $\bar{\mathcal{S}} = \mathcal{S}/\sigma_1$.

The nondimensional velocity of the solid phase, $U_{21} \equiv u_2/c_1$, can be obtained by combining (35) and (40),

$$U_{21} = \frac{2\left[\left(1+\bar{\mathcal{S}}\right)M_s^2 - 1\right]}{(1+\gamma)(1+\bar{\mathcal{S}})M_s}. \tag{41}$$

We note from (41) that U_{21} depends on the non-ideal behavior of the material, also $U_{21} = 0$ when $\sigma_{21} = 1$.

4.1.2. *Model II: Post Compaction Wave for Porosity Very Close to Zero*

In the case of $\theta \to 1$, the assumption that the solid phase is incompressible (i.e., $\rho_1 \neq \rho_2$) can no longer be valid. We thus substitute ρ_1 and ρ_2 in (35)–(37), to obtain

$$\rho_{21} = \frac{-\Lambda\,\sigma_{21} + (1-\Lambda)\bar{\mathcal{S}} + \theta_{12}}{-\Lambda + (1-\Lambda)\bar{\mathcal{S}} + \theta_{21}\,\sigma_{21}}. \tag{42}$$

From (42) we note that $\rho_{21} \to -\Lambda/\theta_{21}$ when $\sigma_{21} \to \infty$ as well as that $\rho_{21} = 1$ when $\sigma_{21} = 1$ and $\theta_{21} = 1$. It is also evident that for the incompressible solid (i.e., $\rho_{21} = 1$), (42) conforms to (38).

Following a procedure similar to the one outlined earlier, the compaction wave Mach number can be calculated from

$$M_s^2 = \frac{(\Lambda-1)\left[(1+\bar{\mathcal{S}})\theta_{21}\,\rho_{21} - (1+\theta_{21}\,\bar{\mathcal{S}})\right]}{\gamma(1+\bar{\mathcal{S}})(1-\theta_{12}\,\rho_{12})(\theta_{21}\,\rho_{21}+\Lambda)}. \tag{43}$$

The solid nondimensional velocity U_{21} can be calculated from

$$U_{21} = \sqrt{\frac{(\Lambda-1)(1-\theta_{12}\,\rho_{12})\left[(1+\bar{\mathcal{S}})\theta_{21}\,\rho_{21} - (1+\theta_{21}\,\bar{\mathcal{S}})\right]}{\gamma(1+\bar{\mathcal{S}})(\theta_{21}\,\rho_{21}+\Lambda)}}. \tag{44}$$

By virtue of (44), $U_{21} = 0$ when $\sigma_{21} = 1$ and $\theta_{21} = 1$.

Table I. Comparison of analytical models with experiments of head-on collision of planar shock waves with rigid porous materials

	Sandusky and Liddiard Experimental Data (1985)	Powers *et al.*'s Model (1989)	Present Model I
θ_2	0.91	0.83	0.83
$\mathcal{D}$	300	340	365
$(\theta\sigma)_2$	3.4×10^7	4.5×10^7	4.74×10^7
ρ_{21}	not available	not available	1*

Table II. Comparison of analytical models with experiments of head-on collision of planar shock waves with rigid porous materials

	Sandusky and Liddiard Experimental Data (1985)	Powers *et al.*'s Model (1989)	Present Model I	Present Model II
θ_2	0.95	0.97	1	1**
$\mathcal{D}$	370	410	365	370
$(\theta\sigma)_2$	5.9×10^7	6.2×10^7	5.71×10^7	5.8×10^7
ρ_{21}	not available	1901/1900	1*	1901/1900

$T_1 = 300\,\mathrm{K}$, $\rho_1 = 1900\,\mathrm{Kg/m^3}$, $C_s = 1500\,\mathrm{J/(Kg\,K)}$
$\mathcal{S} = 8.976 \times 10^6\,\mathrm{m^2/s^2}$, $\gamma = 5$, $\theta_1 = 0.73$, $u_1 = 100\,\mathrm{m/s}$
(*) The model assumes an incompressible solid.
(**) This was imposed as an input.

4.1.3. *Results and Discussion*

The experimental results of Sandusky and Liddiard [45], the predictions of the empirical model proposed by Powers *et al.* [44] and those of our simplified analytical models are shown in Tables I and II, for two cases of different initial conditions.

In the first experiment, the post compaction wave volume fraction of the solid phase was sufficiently less than unity, i.e., $\theta_2 = 0.91$, and hence, only Model I could be used.

In the second experiment, the post compaction wave volume fraction of the solid phase was 0.95. First we applied Model I from which we obtained $\theta_2 \approx 1$. For this reason we decided to apply Model II.

Note that both Models I and II are not as good as the empirical model of Powers *et al.* [44] in predicting θ_2, yet both are much better in predicting $\mathcal{D}$ and $(\theta\sigma)_2$.

We thus conclude:

1. Model II could be practically applied for $\theta_2 \geqslant 0.95$.
2. Using the compaction equation is much more essential when θ_2 is sufficiently less than unity. Dropping this equation when $\theta_2 \to 1$ seems to be justified.
3. The simplified analytical models are sufficient for estimating the post compaction wave properties behind strong compaction waves propagating in air saturated rigid porous materials.

4.2. WEAK WAVES IN GAS SATURATED RIGID POROUS MEDIA

In the following we describe a 1-D, horizontal direction, simple analytical solution for the fluid wave equation. The assumptions used are:

- The solid phase preserves its volume.
- The microscopic solid–fluid interfaces are material with respect to the momentum of both phases.
- There are no external energy sources.
- The conductive and dispersive heat fluxes of the phases is negligible in comparison with their advective heat flux.
- The rate of heat transferred between the fluid and solid phases is negligible.

Based on this conceptual model, we obtain the 1-D balance equations.

We consider the traveling wave propagating, say, in the positive direction of the x-axis. In such a wave all the quantities are functions of $(x - ct)$, where c denotes the linear speed of wave propagation. Thus, the porosity may be represented by the real part of a complex expression

$$\phi = \Re e[A\,\mathrm{e}^{-\mathrm{i}(\omega t - kx)}], \tag{45}$$

where ω denotes the wave frequency and k denotes a displacement factor per unit length. Actually, we can write,

$$c = \left|\frac{\omega}{k}\right| \gg |V_\mathrm{s}|\,. \tag{46}$$

By virtue of (45) and (46), we can confirm a previous assumption, namely,

$$\left|\frac{\partial(1-\phi)}{\partial t}\right| \gg \left|V_\mathrm{s}\frac{\partial(1-\phi)}{\partial x}\right|. \tag{47}$$

Furthermore, the nondimensional form of (47) can be viewed in terms of Strouhal number $\mathrm{St}^e[\equiv L_c^e/(t_c^e V_c^\alpha)]$. Letting $\alpha \equiv \mathrm{s}$ and $e \equiv \phi$, (47) will dictate $\mathrm{St}^\phi \gg 1$. Similarly, letting $e \equiv \mathrm{w_s}$ we may assume

$$\mathrm{St}^{\mathrm{w_s}} \equiv \frac{L_c^{\mathrm{w_s}}}{t_c^{\mathrm{w_s}}\,V_c^\mathrm{s}} \gg 1. \tag{48}$$

We can therefore write

$$V_s = \frac{D_s w_s}{Dt} \cong \frac{\partial w_s}{\partial t}. \tag{49}$$

In view of (11) the definition for the volumetric strain: (47) and (49), we obtain

The solid mass balance equation:

$$\frac{1}{(1-\phi)} \frac{\partial \phi}{\partial t} = \frac{\partial V_s}{\partial x} = \frac{\partial \varepsilon_{sk}}{\partial t} \tag{50}$$

Thus by virtue of (50), V_s and ε_{sk} may be represented in a way similar to (45). Hence, their spatial and temporal changes read

$$\left|\frac{\omega}{k}\right| |\varepsilon_{sk}| = |V_s|. \tag{51}$$

In view of (46) and (51) we conclude that,

$$|\varepsilon_{sk}| \ll 1. \tag{52}$$

Integrating (50) in view of (52) we obtain

$$\frac{1-\phi}{1-\phi_0} = \exp(-\varepsilon_{sk}) \cong 1 - \varepsilon_{sk}, \tag{53}$$

in which we assume that $\varepsilon_{sk\,(x,0)} = 0$ and where ϕ_0 $(= \phi(x,0))$ denotes an initial porosity.

Concerning the fluid's mass and momentum balance equations, we may define 'new' fluid quantities $(\,)_n$, by the following,

$$\rho_n = \phi \rho_f \tag{54}$$

and

$$\frac{\partial P_n}{\partial x} = T_f^* \phi \frac{\partial P}{\partial x}. \tag{55}$$

In view of (54) and (55) we rewrite, respectively, the fluid's mass and momentum balance equations in a form equivalent to Euler's equation describing the propagation of simple (Riemann) fluid waves. These balance equations become

The fluid mass balance equation:

$$\frac{D_f \rho_n}{Dt} + \rho_n \frac{\partial V_f}{\partial x} = 0. \tag{56}$$

The fluid momentum balance equation:

$$\frac{D_f V_f}{Dt} + \frac{1}{\rho_n} \frac{\partial P_n}{\partial x} = 0. \tag{57}$$

Following Landau and Lifshitz [28], and the requirement that the fluid velocity is a function of its density, we can on the basis of (56) or (57) write the pressure wave equation of the 'new' fluid

$$\frac{\partial P_{\mathrm{n}}}{\partial t} + (V_{\mathrm{n}} \pm c_{\mathrm{n}}) \frac{\partial P_{\mathrm{n}}}{\partial x} = 0, \tag{58}$$

where V_{n} and c_{n} denote the 'new' fluid velocity and its sound velocity, respectively, given by

$$V_{\mathrm{n}} = \pm \int_0^{P_{\mathrm{n}}} \frac{\mathrm{d}P_{\mathrm{n}}}{\rho_{\mathrm{n}}\, c_{\mathrm{n}}} \qquad c_{\mathrm{n}} = \pm\sqrt{\frac{\mathrm{d}P_{\mathrm{n}}}{\mathrm{d}\rho_{\mathrm{n}}}}. \tag{59}$$

Note that with the absence of heat exchange between the phases, we regard the motion as being adiabatic for the solid and the fluid. In such a case the specific entropy s_{f}, of the fluid remains constant (i.e., isentropic). Actually, when we assume that the processes of energy dissipation are negligible, we refer to *ideal* fluids, the motion of which must necessarily be adiabatic. By subtracting from the fluid's energy balance equation its mass balance multiplied by s_{f}, we obtain

The fluid energy balance equation:

$$\frac{\mathrm{D_f} s_{\mathrm{f}}}{\mathrm{D}t} = 0. \tag{60}$$

The solid momentum balance equation:

$$\frac{\mathrm{D_s} V_{\mathrm{s}}}{\mathrm{D}t} - \frac{\lambda_{\mathrm{s}}''}{\rho_{\mathrm{s}}(1-\phi)} \frac{\partial^2 \mathrm{w_s}}{\partial x^2} + \frac{\eta}{\rho_{\mathrm{s}}(1-\phi)} \frac{\partial T_{\mathrm{s}}}{\partial x} + \frac{T_{\mathrm{s}}^*}{\rho_{\mathrm{s}}} \frac{\partial P}{\partial x} = 0. \tag{61}$$

The solid energy balance equation:

$$(1-\phi)\rho_{\mathrm{s}}\, C_{\mathrm{s}} \frac{\mathrm{D_s} T_{\mathrm{s}}}{\mathrm{D}t} + \eta T_{\mathrm{s}} \frac{\partial V_{\mathrm{s}}}{\partial x} = 0. \tag{62}$$

4.2.1. *The Isothermal Case*

By virtue of (48) and (49) for the isothermal case we rewrite (61) as

The solid momentum balance equation:

$$\frac{\partial^2 \mathrm{w_s}}{\partial t^2} - c_{\mathrm{s}}^2 \frac{\partial^2 \mathrm{w_s}}{\partial x^2} + \frac{T_{\mathrm{s}}^*}{\rho_{\mathrm{s}}} \frac{\partial P}{\partial x} = 0, \tag{63}$$

where c_{s} denotes the speed of propagation of the displacement wave in the solid phase given by

$$c_{\mathrm{s}}^2 \equiv \frac{\lambda_{\mathrm{s}}''}{\rho_{\mathrm{s}}(1-\phi)}. \tag{64}$$

In view of (63) considering $M_s (\equiv V_s/c_s)$ the solid phase Mach number, we assume that

$$\mathrm{St}_s^w M_s^2 \ll 1, \tag{65}$$

which in view of (48) implies the motion of a *weak wave* ($M_s \ll 1$) and that the solid inertia in (63) is negligible so that the solid momentum balance equation can be approximated by

$$-\frac{\lambda_s''}{(1-\phi)}\frac{\partial \varepsilon_{sk}}{\partial x} + T_s^* \frac{\partial P}{\partial x} = 0. \tag{66}$$

Substituting (53) into (66) when considering (52), we integrate (66) for ε_{sk} and obtain

$$\varepsilon_{sk} = (1-\phi_0)\zeta T_s^* \quad \text{in which} \quad \zeta \equiv \frac{P - P_0}{\lambda_s''} \ll 1, \tag{67}$$

where $\varepsilon_{sk} = 0$ at $P = P_0$. Actually we note that ζ in (67) is negligible for many practical means for example when considering solid porous materials such as SiC or $Al_2\,O_3$. We relate this to the fact that ΔP ($\equiv P - P_0$) is of many orders smaller than λ_s'' as exemplified in the case of a head-on reflection of shock waves (Liepmann and Roshko [37]).

In view of (53), (67) and the compatibility relation in (11), we obtain

$$\phi = \phi_0 + \zeta(1-\phi_0)^2 T_s^* \cong \phi_0, \qquad \mathrm{w}_s = \frac{1-\phi_0}{\lambda_s''} T_s^* \int_{-\infty}^{x} (P - P_0)\,\mathrm{d}x. \tag{68}$$

Based on our findings for the solid phase we can relate the fluid quantities with those of the 'new' fluid. Substituting (68) into (54), by virtue of (67), (55) and assuming that $P_n(x, 0) = 0$ we obtain

$$\rho_n \cong \phi_0\,\rho_f, \qquad P_n \cong \phi_0 (P - P_0) T_f^*. \tag{69}$$

In view of (54), (55), (64) and (68), we expand c_n of (59) and the compressibility β_n of the 'new' fluid can be approximated. These now become

$$c_n^2 \cong T_f^* c_f^2, \qquad \beta_n \cong \frac{\beta_P}{T_s^*[1 - \lambda_s''/(\rho_s\, c_s^2)]}, \tag{70}$$

in which the fluid compressibility β_P ($\equiv (1/\rho_f)\,\mathrm{d}\rho_f/\mathrm{d}P = 1/(\rho_f\, c_f^2)$) is related to its sound velocity. For typical solid density ($\rho_s = 2000\,\mathrm{Kg/m^3}$) and solid sound velocity ($c_s = 7000\,\mathrm{m/s}$), we always have $\lambda_s''/(\rho_s\, c_s^2) > 1$, while $T_s^*/(\beta_P\, \lambda_s'') \ll 1$. We also note that for $\beta_P > 0$ we obtain $\beta_n < 0$.

4.2.2. *The Nonisothermal Case*

Let us first start with the solid phase and assume that

$$\mathrm{St}^{T_s} \equiv \frac{\mathrm{L}_c^{T_s}}{t_c^{T_s}\, V_c^s} \gg 1. \tag{71}$$

Considering (11), (53) and (71), we rewrite (62) the solid energy balance equation in the form

$$(1-\phi_0)\rho_s C_s \frac{\partial T_s/\partial t}{T_s} + \eta \frac{\partial \varepsilon_{sk}/\partial t}{(1-\varepsilon_{sk})} = 0, \tag{72}$$

from which, by virtue of (52), we obtain,

$$T_s = T_{s_0}\left[1 - \frac{\eta \varepsilon_{sk}}{(1-\phi_0)\rho_s C_s}\right], \tag{73}$$

where T_{s_0} denotes the solid temperature at $\varepsilon_{sk} = 0$.

In view of (11), (48), (49), (53), (65) and (73), we approximate (61) the solid momentum balance equation, to read

$$\frac{\lambda_{\mathrm{eff}}}{(1-\phi_0)(1-\varepsilon_{sk})} \frac{\partial}{\partial x}(1-\varepsilon_{sk}) = T_s^* \frac{\partial P}{\partial x} \tag{74}$$

in which

$$\lambda_{\mathrm{eff}} \equiv \left[1 + \frac{T_{s_0}\alpha_s^2 \lambda_s''}{(1-\phi_0)\rho_s C_s}\right]\lambda_s'' \cong \lambda_s'', \tag{75}$$

where α_s denotes the thermal expansion coefficient (related to η the thermal stress coefficient, i.e., $\eta = \alpha_s \lambda_s''$). The approximation in (75) is possible for thermoelastic rigid materials (e.g., SiC or Al_2O_3) and when considering the appropriate order of magnitudes, i.e., $\lambda_s'' \cong 400\,\mathrm{GPa}$, $T_{s_0} = 300\,\mathrm{K}$, $\alpha_s = 5\times10^{-6}\,\mathrm{K}^{-1}$, $C_s = 1000\,\mathrm{J/Kg/K}$, $\rho_s = 2000\,\mathrm{Kg/m^3}$ and $0 < \phi_0 < 1$.

Solving (74) in view of (52) and assuming that $P = P_0$ at $\varepsilon_{sk} = 0$ yields

$$\varepsilon_{sk} \cong \frac{(1-\phi_0)T_s^*}{\lambda_{\mathrm{eff}}}(P - P_0). \tag{76}$$

In view of (75) and (76) when substituted into (73), for different values of ρ_s it is evident that practically

$$T_s \cong T_{s_0}. \tag{77}$$

When substituting (76) into (53) we obtain

$$\phi = \phi_0 + \frac{(1-\phi_0)^2 T_s^*}{\lambda_{\mathrm{eff}}}(P - P_0). \tag{78}$$

Accordingly, using (76) and referring to (11), the compatibility equation, we write,

$$\mathrm{w_s} = \frac{1-\phi_0}{\lambda_{\mathrm{eff}}} T_{\mathrm{s}}^* \int_{-\infty}^{x} (P - P_0)\,\mathrm{d}x. \tag{79}$$

Concerning the fluid phase, we need to address six variables (ϕ, ρ_{f}, P, T_{f}, V_{f}, s_{f}). For these we have three balance equations, (56), (57), (60), and (78) a relation for the porosity. We thus add constitutive laws assuming that these macroscopic forms are similar to their microscopic counterparts while the coefficients (to be determined experimentally) are different in value from those of the microscopic ones. For an *ideal fluid* we can thus add the relation

$$\left(\frac{P}{P_0}\right)\left(\frac{\rho_{\mathrm{f_0}}}{\rho_{\mathrm{f}}}\right)^{C_{\mathrm{f}}/C_{\mathrm{P}}} = \exp\left(\frac{s_{\mathrm{f}} - s_{\mathrm{f_0}}}{C_{\mathrm{f}}}\right), \tag{80}$$

where $\rho_{\mathrm{f_0}}$ and $s_{\mathrm{f_0}}$ are reference values obtained when $P = P_0$ and C_{P} denotes the fluid specific heat at constant pressure. We also write the equations of state for a perfect gas in the form

$$\rho_{\mathrm{f}} = \frac{P}{RT_{\mathrm{f}}}, \tag{81}$$

in which R denotes the specific gas constant.

Substituting (78) into (55), integrating, and in view of (80) we obtain

$$P_{\mathrm{n}} = \left[A + \tfrac{1}{2}B(P - P_0)\right](P - P_0) \cong A(P - P_0), \tag{82}$$

where

$$A \equiv \phi_0 T_{\mathrm{f}}^* \quad \text{and} \quad B \equiv \frac{(P - P_0)^2 T_{\mathrm{f}}^* T_{\mathrm{s}}^*}{\lambda_{\mathrm{eff}}} \ll 1. \tag{83}$$

We note that in view of the approximation expressed in (75), B is practically negligible and P_{n} is approximated, accordingly. We can rewrite ϕ in terms of P_{n}, this in view of (78), (82) and (83) becomes

$$\phi = \frac{\sqrt{A^2 + 2BP_{\mathrm{n}}}}{T_{\mathrm{f}}^*} \cong \phi_0. \tag{84}$$

We note that the approximate forms of (82) and (84) are in line with the isothermal case. By virtue of (54), (82) and (83), we can also rewrite the constitutive relation (80) in the form

$$\begin{aligned}\exp\left(\frac{s_{\mathrm{f}} - s_{\mathrm{f_0}}}{C_{\mathrm{f}}}\right) &= \left(\frac{\sqrt{A^2 + 2BP_{\mathrm{n}}} - A}{BP_0}\right)\left(\frac{\sqrt{A^2 + 2BP_{\mathrm{n}}}}{T_{\mathrm{f}}^*}\frac{\rho_{\mathrm{f_0}}}{\rho_{\mathrm{n}}}\right)^{C_{\mathrm{P}}/C_{\mathrm{f}}} \\ &\cong \left(1 + \frac{1}{A}\frac{P_{\mathrm{n}}}{P_0}\right)\left(\phi_0 \frac{\rho_{\mathrm{f_0}}}{\rho_{\mathrm{n}}}\right)^{C_{\mathrm{P}}/C_{\mathrm{f}}}.\end{aligned} \tag{85}$$

Altogether, we now face four (ρ_n, V_f, P_n, s_f) variables. To solve for these variables, we have three balance equations (56), (57), (60) and a constitutive relation (85). It is noteworthy to find an expression for the temperature T_n, of the generalized fluid. This will also allow us to write the generalized state function commencing from (81).

We start by introducing the relation for the generalized enthalpy $h_n(P_n, s_f)$. Using the definition for the enthalpy we postulate that

$$\mathrm{d}h_n = T_n\,\mathrm{d}s_f + \frac{\mathrm{d}P_n}{\rho_n}, \tag{86}$$

from which we have

$$\frac{1}{\rho_n} = \frac{\partial h_n}{\partial P_n} \quad \text{and} \quad T_n = \frac{\partial h_n}{\partial s_f}. \tag{87}$$

In view of (54), (55), (86) and (87) we obtain

$$h_n(P_n, s_f) = T_f^* h(P, s_f) \tag{88}$$

and

$$T_n = T_f^* T_f. \tag{89}$$

The equation of state of the generalized fluid may now be obtained from (54), (82)–(84), (89) when substituted into (81)

$$\rho_n = \frac{\sqrt{A^2 + 2BP_n}\left(BP_0 - A + \sqrt{A^2 + 2BP_n}\right)}{BRT_n} \cong \frac{AP_0}{RT_n}. \tag{90}$$

Hence, we note that the density of the generalized fluid becomes dependent only on the temperature of this fluid.

In what follows we will describe the roll of Forchheimer terms by comparing shock tube experiments and numerical simulation of compaction waves traveling through a 1-D saturated thermoelastic porous medium.

5. Numerical Solution for Compaction Waves in a 1-D Saturated Thermoelastic Porous Medium

During the second time interval, compaction wave equations are formed. The 1-D balance equations of mass, momentum and energy of the fluid ((1), (23) and (25), respectively) and of the solid ((2), (24) and (26), respectively) when written in a vector form (Levy *et al.* [34]) become

$$\frac{\partial \mathbf{U}}{\partial t} + \frac{\partial \mathbf{F}}{\partial x} = \mathbf{Q}. \tag{91}$$

The variables vector $\mathbf{U}$, is defined by

$$\mathbf{U} = [r_f, r_s, m_f, m_s, E_f, E_s]^{\mathrm{T}}, \tag{92}$$

where

$$
\begin{aligned}
&r_{\mathrm{f}} \equiv \phi\rho_{\mathrm{f}}, \quad m_{\mathrm{f}} \equiv r_{\mathrm{f}} V_{\mathrm{f}}, \quad E_{\mathrm{f}} \equiv r_{\mathrm{f}} e_{\mathrm{f}} = r_{\mathrm{f}}\left(C_{\mathrm{f}} T_{\mathrm{f}} + \frac{V_{\mathrm{f}}^2}{2}\right), \\
&r_{\mathrm{s}} \equiv (1-\phi)\rho_{\mathrm{s}}, \quad m_{\mathrm{s}} \equiv r_{\mathrm{s}} V_{\mathrm{s}}, \quad E_{\mathrm{s}} \equiv r_{\mathrm{s}} e_{\mathrm{s}} = r_{\mathrm{s}}\left(C_{\mathrm{s}} T_{\mathrm{s}} + \frac{V_{\mathrm{s}}^2}{2}\right),
\end{aligned}
\tag{93}
$$

e_α denotes the total energy per mass unit of the α phase. The flux vector $\mathbf{F}$, is given by

$$
\mathbf{F} = \begin{bmatrix}
m_{\mathrm{f}} \\
m_{\mathrm{s}} \\
\dfrac{m_{\mathrm{f}}^2}{r_{\mathrm{f}}} + T_{\mathrm{f}}^* \phi P \\
\dfrac{m_{\mathrm{s}}^2}{r_{\mathrm{s}}} - \sigma_{\mathrm{s}}' + \left(1 - \phi T_{\mathrm{f}}^*\right) P \\
\dfrac{m_{\mathrm{f}}}{r_{\mathrm{f}}}\left(E_{\mathrm{f}} + T_{\mathrm{f}}^* \phi P\right) \\
\dfrac{m_{\mathrm{s}}}{r_{\mathrm{s}}}[E_{\mathrm{s}} - \sigma_{\mathrm{s}}' + (1 - \phi T_{\mathrm{f}}^*) P]
\end{bmatrix}.
\tag{94}
$$

The source vector $\mathbf{Q}$, is given by

$$
\mathbf{Q} = \begin{bmatrix}
0 \\
0 \\
T_{\mathrm{f}}^* P \dfrac{\partial \phi}{\partial x} - \tilde{F} r_{\mathrm{f}} \left|\dfrac{m_{\mathrm{f}}}{r_{\mathrm{f}}} - \dfrac{m_{\mathrm{s}}}{r_{\mathrm{s}}}\right| \left(\dfrac{m_{\mathrm{f}}}{r_{\mathrm{f}}} - \dfrac{m_{\mathrm{s}}}{r_{\mathrm{s}}}\right) \\
-T_{\mathrm{f}}^* P \dfrac{\partial \phi}{\partial x} + \tilde{F} r_{\mathrm{f}} \left|\dfrac{m_{\mathrm{f}}}{r_{\mathrm{f}}} - \dfrac{m_{\mathrm{s}}}{r_{\mathrm{s}}}\right| \left(\dfrac{m_{\mathrm{f}}}{r_{\mathrm{f}}} - \dfrac{m_{\mathrm{s}}}{r_{\mathrm{s}}}\right) \\
\dfrac{m_{\mathrm{s}}}{r_{\mathrm{s}}}\left[T_{\mathrm{f}}^* P \dfrac{\partial \phi}{\partial x} - \tilde{F} r_{\mathrm{f}} \left|\dfrac{m_{\mathrm{f}}}{r_{\mathrm{f}}} - \dfrac{m_{\mathrm{s}}}{r_{\mathrm{s}}}\right| \left(\dfrac{m_{\mathrm{f}}}{r_{\mathrm{f}}} - \dfrac{m_{\mathrm{s}}}{r_{\mathrm{s}}}\right)\right] \\
\dfrac{m_{\mathrm{s}}}{r_{\mathrm{s}}}\left[-T_{\mathrm{f}}^* P \dfrac{\partial \phi}{\partial x} + \tilde{F} r_{\mathrm{f}} \left|\dfrac{m_{\mathrm{f}}}{r_{\mathrm{f}}} - \dfrac{m_{\mathrm{s}}}{r_{\mathrm{s}}}\right| \left(\dfrac{m_{\mathrm{f}}}{r_{\mathrm{f}}} - \dfrac{m_{\mathrm{s}}}{r_{\mathrm{s}}}\right)\right]
\end{bmatrix},
\tag{95}
$$

in which $\tilde{F}$ denotes the Forchheimer coefficient for an isotropic solid matrix. The pressure P, is prescribed by the equation of state

$$
\phi P = (\gamma - 1)\left(E_{\mathrm{f}} - \frac{m_{\mathrm{f}}^2}{2 r_{\mathrm{f}}}\right),
\tag{96}
$$

where γ denotes the specific heat capacity ratio of the fluid phase.

The porosity ϕ, and the skeleton strain ε_{sk}, can be expressed as

$$
\phi = 1 - \frac{r_{\mathrm{s}}}{\rho_{\mathrm{s}}}, \qquad \varepsilon_{sk} = 1 - \frac{r_{\mathrm{s}}}{r_{\mathrm{s}0}}.
\tag{97}
$$

In view of (10) we can express the constitutive relation for the effective stress σ_s', in the form

$$\sigma_s' = E_\varepsilon\left(\frac{r_{s0}-r_s}{r_{s0}}\right) - E_T\left(\frac{E_s}{r_s} - \frac{E_{s0}}{r_{s0}} - \frac{m_s^2}{2r_s^2} + \frac{m_{s0}^2}{2r_{s0}^2}\right), \tag{98}$$

in which $E_\varepsilon(\equiv \lambda_s'' + \mu_s')$, $E_T(\equiv \eta/C_s)$ are the one-dimensional macroscopic Lame coefficients for a thermoelastic solid and the subscript $(\,)_{s0}$ denotes the solid properties at an initial state.

The set (91) of six partial differential governing equations defined by (92), (94) and (95) are to be solved for six unknowns namely, r_f, r_s, m_f, m_s, E_f and E_s. Consequently, in principle given the appropriate conditions, the set is complete and can be solved. However, due to the complexity of the equations, an analytical solution of the set is not feasible. Instead, a numerical solution has been performed.

Note that in writing (91) we assumed that the gradients of the porosity were very small and therefore they might be written as source terms in the source vector $\mathbf{Q}$, given by (95). As a result the source vector $\mathbf{Q}$, contains derivative terms and thus affects the character of the equations (hyperbolic rather than elliptic-hyperbolic). This is very convenient for numerical purposes and is correct only when the gradients of the porosity are very small as is the case in this study. Applying this procedure removes the ill-posedness associated with the elliptic-hyperbolic character of the equations which is usually manifested in highly oscillatory solutions as the mesh is refined.

The numerical scheme for solving (91) is based on an upwind *TVD* shock-capturing scheme, originally developed by Harten [23], which was extended to solve the problem of compaction waves propagation in saturated thermoelastic porous media.

6. Experimental Study

The head-on collision of planar shock waves with rigid porous materials was investigated experimentally in order to validate the predictions of the physical model and the numerical code. The experiments were conducted in a 75 mm $\times$ 75 mm shock tube. The incident shock wave Mach number range was $1.2 \leqslant M_i \leqslant 1.7$, the initial pressures and temperatures throughout the experimental study were about 830 mbar and 288 K, respectively.

The rigid porous samples were made of silicon carbide (SiC) and alumina (Al_2O_3). The SiC manufactured porous material had either 10 or 20 pores per inch and the Al_2O_3 manufactured porous material had either 30 or 40 pores per inch. The porosity of these porous materials as well as the initial length L_0, of the samples which were cut from these materials are given in Table III. The porosity ϕ, was simply calculated from $\phi = 1 - \rho_b/\rho_s$, where ρ_b is the bulk density of the porous material and ρ_s the material density of the skeleton of which the porous material is made. Note that the above expression is limited to gas saturated porous materials as was the case in the present study. The cross-section dimensions of the samples

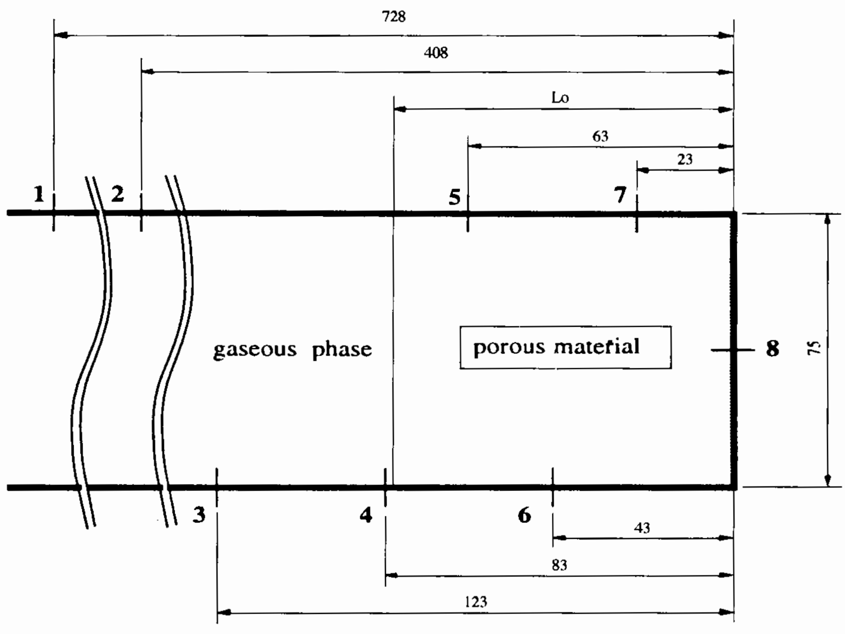

Figure 1. Schematic illustration of the experimental set-up and the location of the pressure transducers (numbered 1 to 8).

were 75 mm × 75 mm and hence, as a result of the head-on collision with the shock wave they underwent a uni-axial strain (also known as tri-axial stress) compression. Twelve experiments were conducted with each sample. The samples were mounted at the end of the driven section of the shock tube in such a way that their back edges were supported by the shock-tube end-wall.

A schematic illustration of the experimental set-up used during the course of the experimental study is shown in Figure 1. Seven pressure transducer ports were used in each experiment. The pressure transducers in ports 1 and 2 were used to measure the incident shock wave velocity. Pressure transducers were mounted in ports 4, 5, 6, 7 and 8 for the samples having an initial length up to (inclusive) 83 mm (see Table III). For the alumina sample with an initial length of 99 mm the pressure transducer of port 4 was moved to port 3. This was done in order to have a measurement of the pressure changes caused by the shock wave which reflected backwards from the front edge of the porous material.

7. Comparison Between the Numerical Predictions and the Experimental Results

In order to validate the physical model and the numerical code, the governing equations were solved numerically for different samples and a variety of initial conditions and compared to experimental results. In order to solve the governing equations and compare the solution to the experimental results, the various parameters which appear in the physical model namely: the macroscopic Lame coefficients for a thermoelastic solid E_ε and E_T, the Forchheimer factor $\tilde{F}$, the fluid tortuosity T_f^*, and the intrinsic density of the solid matrix ρ_s, which appear in the physical model had to be estimated for each sample. Based on the properties of the materials of which the samples were made of and the fact that the upper limit of the elastic stress reduces when the porosity increases, in a $(1-\phi)^2$ manner, Gibson and Ashby [19], the magnitudes of the macroscopic Lame coefficients E_ε and E_T, were estimated to be identical for all the samples:

$$E_\varepsilon = 380 \times 10^7 \text{ Pa} \quad \text{and} \quad E_T = 26.207 \text{ Kg/m}^3.$$

The intrinsic density of the solid matrix for all the samples (SiC and Al_2O_3), as provided by the manufacturer, was

$$\rho_s = 2000 \pm 60 \text{ Kg/m}^3.$$

The tortuosity factors T_f^*, for the various samples were found by estimating the ratio between the speed of sound of the air inside the porous medium a_f and that in pure air a (Li *et al.* [36]),

$$\left(\frac{a_f}{a}\right)^2 = \frac{\left(1 - T_f^* + \gamma T_f^*\right) T_f^*}{\gamma}. \tag{99}$$

The Forchheimer factors $\tilde{F}$, for the various samples where found experimentally. In these experiments, each sample was mounted in a pipe and the pressure drop across it was measured as a function of the air flow rate. The pressure drop was found to be a parabolic function of the air velocity. This was done by assuming that the pressure drop depends linearly on the length of the sample. The values of the tortuosity and the Forchheimer factors, as obtained experimentally for the various samples, are presented in Table III.

In order to validate the physical model, (91) was solved numerically for different samples and initial conditions and compared to experimental results. Table IV represents the initial conditions of 18 different experiments. The comparison between the

Table III. The Forchheimer ($\tilde{F}$) and the tortuosity (T_f^*) factors, porosity (ϕ) and sample length (L_0) for the different samples

Sample material	Sample type	Pores per inch (ppi)	$\tilde{F}$ (1/m)	T_f^*	ϕ	L_0 (mm)
Silicon carbide	I	10	300	0.7	0.728 ± 0.016	40, 60, 81
(SiC)	II	20	500	0.7	0.745 ± 0.001	41, 62, 83
Alumina	III	30	900	0.75	0.814 ± 0.010	48, 93
(Al_2O_3)	IV	40	1800	0.75	0.821 ± 0.007	50, 99

Table IV. The initial conditions for the various experiments

Test number	Sample material	Sample length [mm]	Initial pressure (KPa)	Initial temperature (K)	Shock Mach number-M_i
1		40	83.04	290.0	1.378
2	SiC	60	83.11	290.5	1.385
3		81	83.41	290.5	1.377
4	10 ppi	81	83.71	289.5	1.543
5		81	83.70	290.5	1.734
11		48	82.84	292.0	1.374
12	Al_2O_3	93	83.41	290.5	1.377
13	30 ppi	93	83.36	291.0	1.539
14		93	83.12	291.5	1.744
15		50	83.09	292.0	1.374
16	Al_2O_3	50	83.08	292.5	1.545
17	40 ppi	50	83.10	292.5	1.741
18		99	83.16	290.5	1.377

predictions of the numerical simulations and the experimental results, for all the cases appearing in Table IV. In what follows, we will present two of these comparisons the experiments of which are listed in Table IV as test numbers 1 and 13.

Figures 2(a)–(e) and 3(a)–(e) represent typical experimental results and their numerical simulations for SiC and Al_2O_3 samples, respectively. P_1 is the pressure ahead of both the incident and the transmitted shock waves, P_2 is the theoretical pressure which should have been reached behind the incident shock wave, and P_5 is the theoretical pressure which should have been reached had the incident shock wave reflected head-on from a solid surface. The symbols represent the experimental results, the solid lines are the numerically predicted values when accounting for Forchheimer terms and the dash-dot lines represent the simulations without Forchheimer terms. The pressure histories of the pure gas just ahead of the front edge of the porous sample are shown in Figure 2(a); Figure 2(b) for the SiC and Figure 3(a) for the Al_2O_3. The pressure histories of the gas occupying the pores of the porous material along the shock tube side-wall and at its end-wall are shown in Figures 2(c)–(e) for the SiC samples and Figures 3(a)–(e) for the Al_2O_3 samples.

Figures 2 and 3, clearly emphasize the advantage of simulations with Forchheimer terms in retrieving the experimental observations. Major differences between the two cases are evident. While the simulations without Forchheimer terms, (dashed doted lines) do not agree with the experimental results, simulations with Forchheimer terms (solid lines) results in predictions which excellently reproduce the experiments. When Forchheimer terms are neglected the shock waves which are reflected, head-on, from the front edge of the porous sample, are weaker than those obtained when the Forchheimer terms are accounted for (compare the second jump in pressure traces

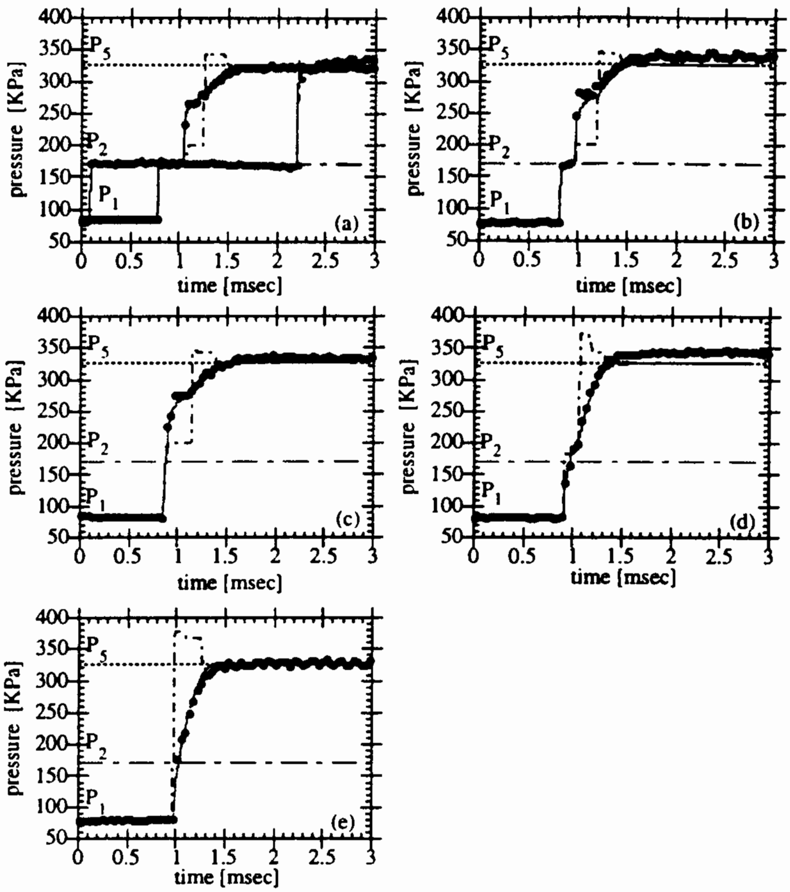

Figure 2. Typical experimental results and their numerical simulations with a 40 mm long sample made of SiC having 10 pores per inch (sample I in Table III). The incident shock wave Mach number in this experiment was $M_i = 1.378$ (test number 1 in Table IV). The pressure histories of the pure gas just ahead of the front edge of the porous material are shown in Figures 2(a) and 3(b). The pressure histories of the gas occupying the pores of the porous material along the shock tube side-wall and at its end-wall are shown in Figures 2(c)–(e), respectively. The symbols represent the experimental results, the solid lines are the numerically predicted values when accounting for Forchheimer terms and the dash-dot lines represent the simulations without Forchheimer terms. P_1 is the pressure ahead of both the incident and the transmitted shock waves, P_2 is the theoretical pressure which should have been reached behind the incident shock wave, and P_5 is the theoretical pressure which would have been reached had the incident shock wave reflected head-on from a solid end-wall.

shown in Figures 2(a), 2(b) and 3(a)). These figures also indicate that when the Forchheimer terms are neglected, a sharp shock wave is transmitted at a later time from the porous material into the gaseous phase resulting in a third jump in pressure longer than P_5. These high pressures are later decayed by the transmitted expansion waves and reach as expected the value of P_5.

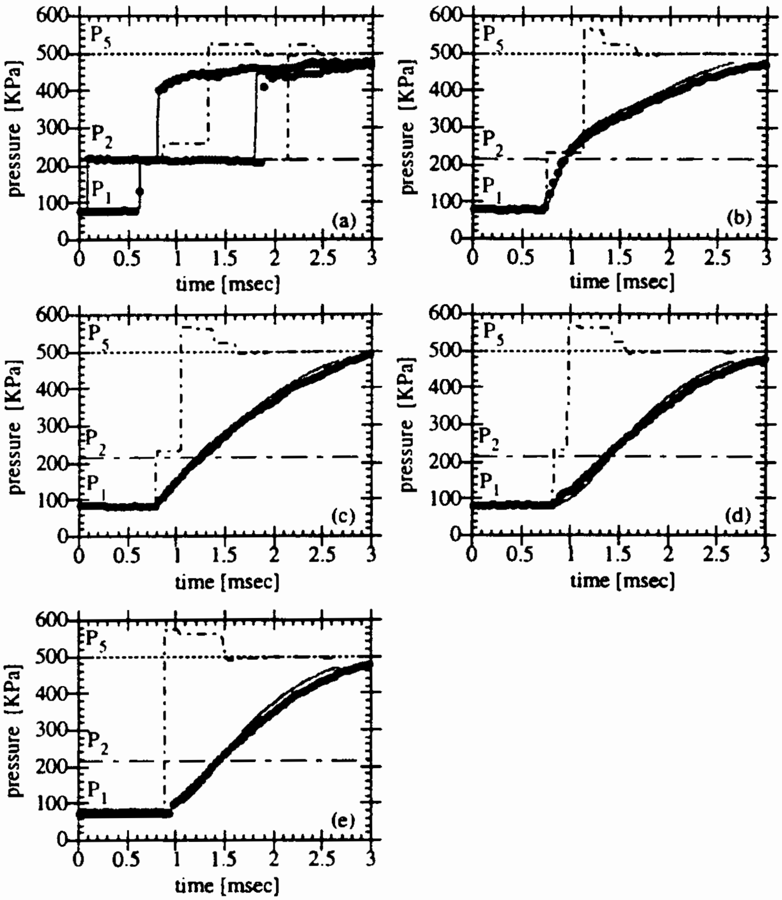

Figure 3. Typical experimental results and their numerical simulations with a 93 mm long sample made of Al_2O_3 having 30 pores per inch (sample III in Table III). The incident shock wave Mach number in this experiment was $M_i = 1.539$ (test number 13 in Table IV). The pressure histories of the pure gas just ahead of the front edge of the porous material are shown in Figure 3(a). The pressure histories of the gas occupying the pores of the porous material along the shock tube side-wall and at its end-wall are shown in Figures 3(b)–(e), respectively. The symbols represent the experimental results, the solid lines are the numerically predicted values when accounting for Forchheimer terms and the dash-dot lines represent the simulations without Forchheimer terms. P_1, P_2 and P_5 are defined in the caption of Figure 2.

In addition, as a result of the neglection of the Forchheimer terms, the shock waves which are transmitted into the porous material samples do not develop a dispersed structure, as is the situation in reality. Instead, they maintain their sharp fronts. The fact that the transmitted shock waves maintain their sharp structure result in a jump to pressures larger than P_2 behind them (see the sharp jumps in the pressures inside the porous samples in Figures 2(c), 2(d), 3(c) and 3(d)). Figures 2(e) and 3(e) in which the pressure histories at the back edge of the porous samples (that is at the shock tube end-wall) are shown again, indicate that when the Forchheimer terms are neglected, in contrast to the experimental results, sharp shock waves reach the end-wall. The reason for the above-mentioned differences lies in the fact that the Forchheimer terms emphasize the friction between the two phases and as a result increase the rate of momentum exchange. This, in turn, results in a situation in which much larger impulses $\int P \, dt$, are predicted numerically when the Forchheimer terms are neglected.

It is clearly evident from these comparisons that the agreement between the experimental results and the numerical predictions is very good. Note that there are disagreements between the numerical and the experimental positions of the reflected shock wave after it traveled to a relatively long distance from the front edges of the samples (see Figures 2(a) and 3(a)). The agreement regarding the reflected shock wave position was better in the case of low incident shock wave Mach numbers and short samples. This may be caused by the way the porosity gradient terms were treated in the source vector $\mathbf{Q}$.

Although Figures 2(a)–(e) and 3(a)–(e) describe the results of only two typical experiments, one in the SiC sample and one in an alumina (Al_2O_3) sample, similar good to excellent agreements were obtained in the comparisons with all the experiments which were conducted by Levy [29].

8. Sensitivity Analysis

The developed macroscopic model also accounts for geometrical properties. Hence, for example, the speed of the wave is not only based on properties of the phases but also a function of the porous material structure. Some macroscopic parameters which resulted from the averaging process were the tortuosity factor which represents a tensor associated with the matrix directional cosines, the hydraulic radius of the pore spaces and the porosity which represents the volume fraction of the pores filled by the fluid. As was also shown, a most important factor is the Forchheimer tensor accounting for the microscopic inertia exchange between the phases at the solid/fluid interface. In what follows, we will present a 1-D numerical parametric study of the flow field which develops when a planar shock wave strikes a rigid porous material head-on. This is done in terms of studying the effect of the tortuosity, Forchheimer and Lamé coefficients and the initial porosity in the case of a 81 mm long sample of SiC and an incident shock wave having a Mach number $M_i = 1.377$.

8.1. THE TORTUOSITY EFFECT

The dependence of the pressure field on the tortuosity is shown in Figures 4(a)–(c). It is evident from Figure 4(a) that the compression (shock) wave velocity increases as the tortuosity increases. It also indicates that the pressure rise is faster when the tortuosity is larger. It is evident from Figure 4(c) that the reflected shock wave moves faster when the tortuosity is smaller.

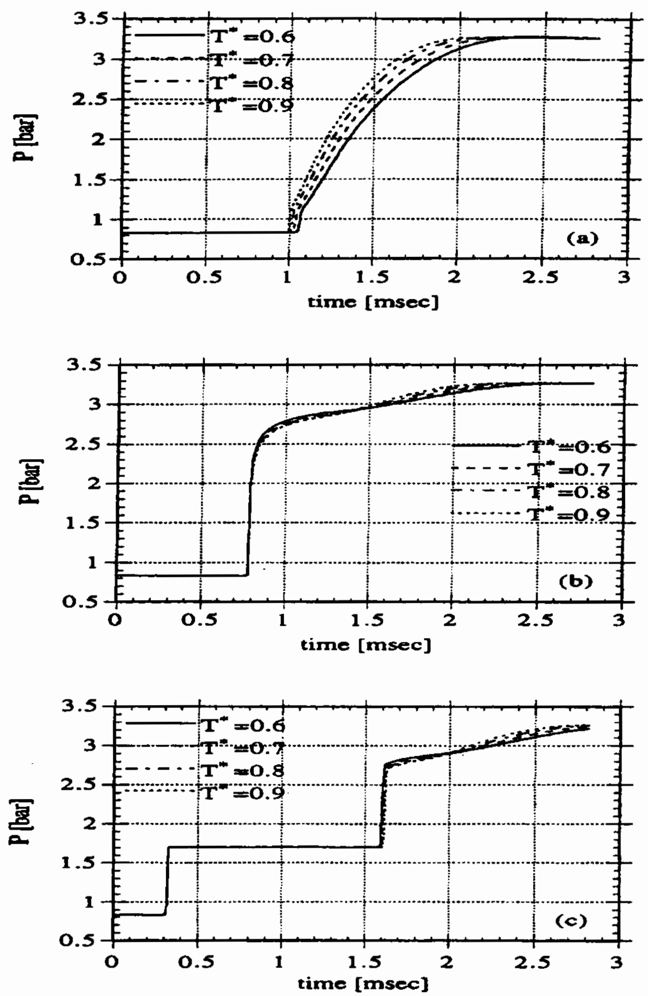

Figure 4. The influence of the tortuosity on the pressure: (a) at the back edge of the sample, (b) at the front edge of the sample and (c) 42 cm ahead of the sample. The sample was made of SiC and it was 81 mm long. The incident shock wave Mach number was $M_i = 1.377$.

The influence of the tortuosity on the fluid velocity, at the front edge and ahead of the sample, is shown in Figures 5(a) and 5(b), respectively. We note that the final velocity values become larger for smaller tortuosities.

It is important to note here that two waves are transmitted into the porous material when the incident shock wave strikes it. The first is a very rapid compaction wave which propogates in the solid matrix, and the second is a compression (shock) wave which propagates through the gaseous phase occupying the pores. These waves interact at the solid/fluid interfaces of the porous material. The compaction wave, which is very fast, is responsible for the fast porosity changes.

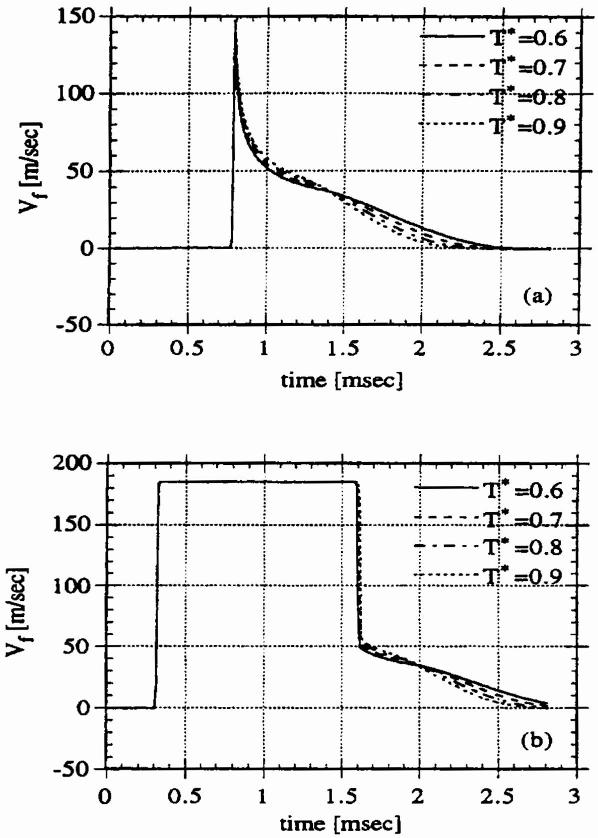

Figure 5. The influence of the tortuosity on the fluid velocity: (a) at the front edge of the sample and (b) 42 cm ahead of the sample. The sample was made of SiC and it was 81 mm long. The incident shock wave Mach number was $M_i = 1.377$.

Although not demonstrated, we concluded that practically the porosity could be assumed to be constant and independent of the tortuosity.

Similarly, the solid matrix velocity was found to be practically independent of the tortuosity. Smaller tortuosities result in larger normal stress. However, given enough time after the initiation of the interaction the finally obtained normal stresses becomes independent of the tortuosity.

8.2. THE FORCHHEIMER FACTOR EFFECT

The dependence of the pressure field on the Forchheimer factor is depicted in Figures 6(a)–(c). We note from Figure 6(a) that the compression (shock) wave velocity is not influenced by the Forchheimer factor as the profiles for the various Forchheimer factors start to rise at the same time. The finally obtained pressure is also seen to be independent of the Forchheimer factor. However, the pressure rises faster

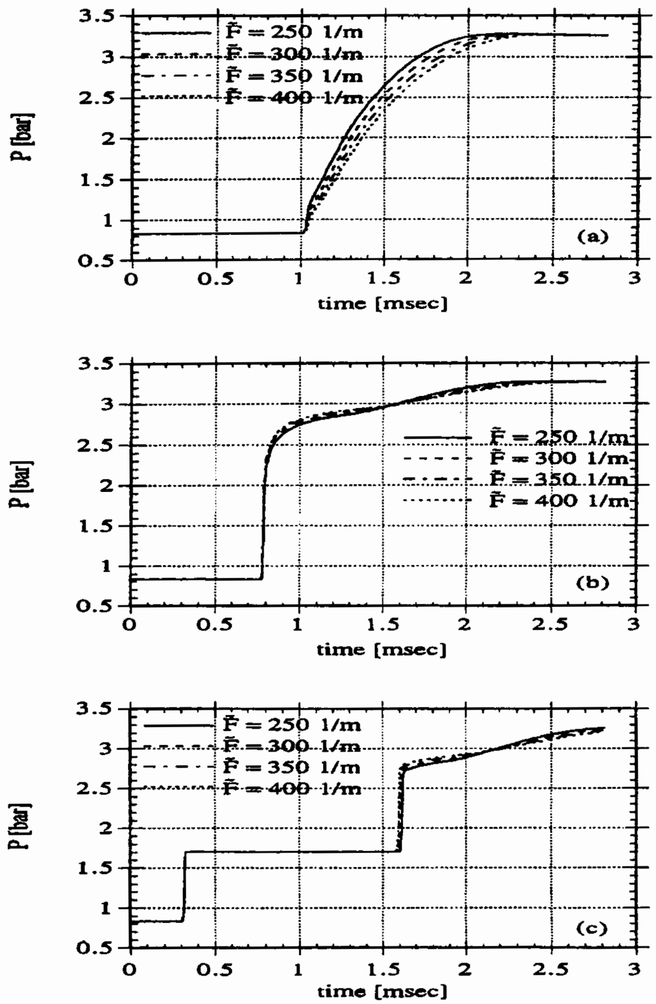

Figure 6. The influence of the Forchheimer coefficient on the pressure: (a) at the back edge of the sample, (b) at the front edge of the sample and (c) 42 cm ahead of the sample. The sample was made of SiC and it was 81 mm long. The incident shock wave Mach number was $M_i = 1.377$.

for smaller Forchheimer factors. Figures 6(b) and 6(c) demonstrate, respectively, that the pressures at the front edge of the sample and ahead of it are less influenced by the Forchheimer factor.

In view of Figure 7 we note that different Forchheimer factors can result in fluid velocity differences of up to 7 m/s (for example at about 1 and 2 ms in Figure 7(a)). However, the finally obtained fluid velocities are independent of the Forchheimer factor.

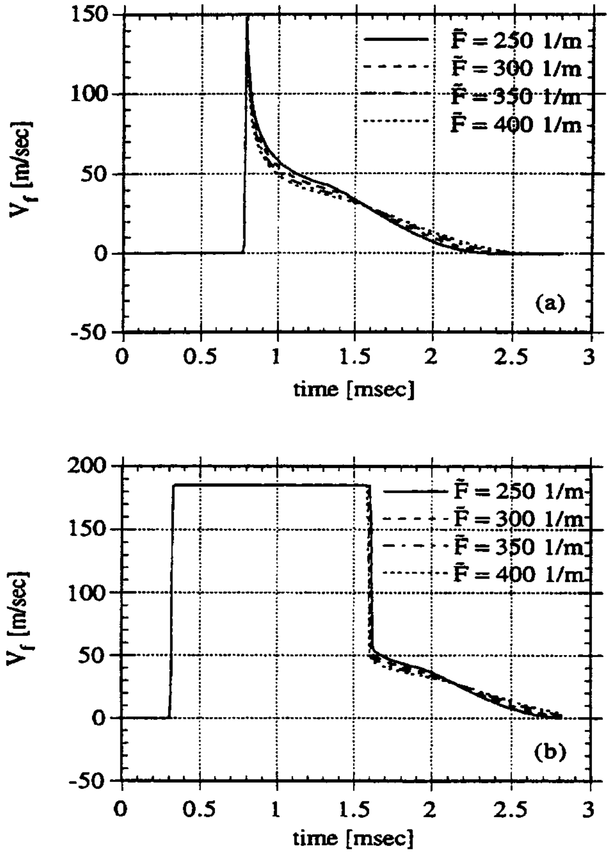

Figure 7. The influence of the Forchheimer coefficient on the fluid velocity: (a) at the front edge of the sample and (b) 42 cm ahead of the sample. The sample was made of SiC and it was 81 mm long. The incident shock wave Mach number was $M_{\mathrm{i}} = 1.377$.

8.3. THE EFFECT OF THE LAMÉ COEFFICIENTS

The effect of the Lamé $E_\varepsilon (\equiv \lambda_s'' + \mu_s')$ coefficient was most noticeable on the normal stress profiles (Figure 8). It is demonstrated that the normal stresses reach higher values for the smallest value of E_ε. In addition, the finally obtained values of the normal stress are constant and they are independent of E_ε. It should also be noted that the compression (shock) wave reaches the back edge of the sample faster for larger values of E_ε. The difference in the time of arrival between $E_\varepsilon = 380 \times 10^8$ Pa and $E_\varepsilon = 380 \times 10^8$ Pa is about 90 ms.

8.4. THE INITIAL POROSITY EFFECT

A significant dependence on the initial porosity was exhibited for the normal stress distribution (Figure 9). Larger porosity values, yield higher normal stresses. For

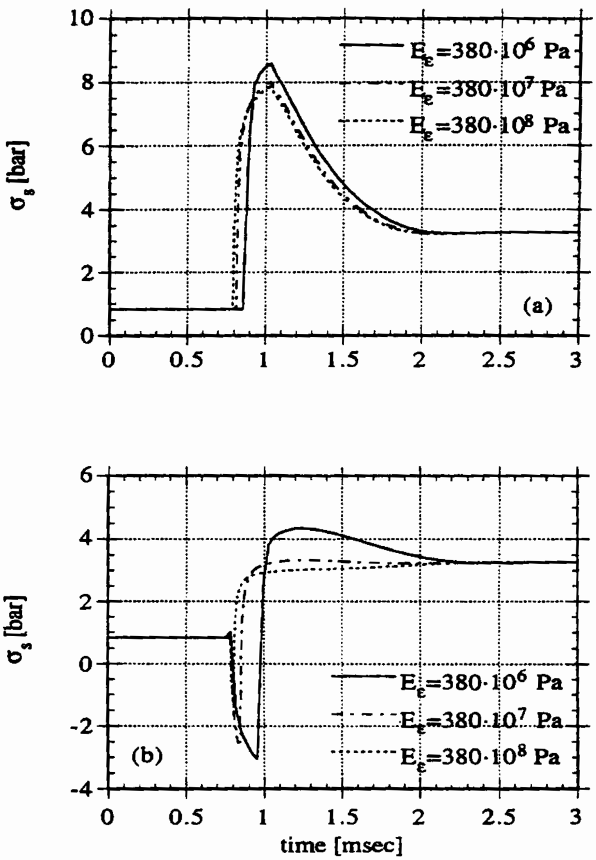

Figure 8. The influence of the E_ε $\left(\equiv \lambda_s'' + \mu_s'\right)$ Lamé coefficient on the normal stress: (a) at the back edge of the sample and (b) at the front edge of the sample. The sample was made of SiC and it was 81 mm long. The incident shock wave Mach number was $M_\text{i} = 1.377$.

example, Figure 9(a) indicates that at the rear edge for $\phi_0 = 0.68$ we obtain $(\sigma_\text{s})\text{max} \approx 6.9$ KPa while $\phi_0 = 0.78$ yields $(\sigma_\text{s})\text{max} \approx 9.5$ KPa.

9. Conclusions

Macroscopic balance equations of mass, momentum and energy are described for the case of saturated thermoelastic porous media.

We show that microscopic terms of momentum should be accounted for at the interfaces between the solid and the fluid phases. These microscopic terms lead to the macroscopic Forchheimer terms. The macroscopic terms, represent sources of momentum and energy that are exchanged between the fluid phases and the solid phase, at their solid–fluid interfaces.

In the case of the phases momentum balance equation we present a separate momentum balance equation for the fluid accounting for momentum flux terms,

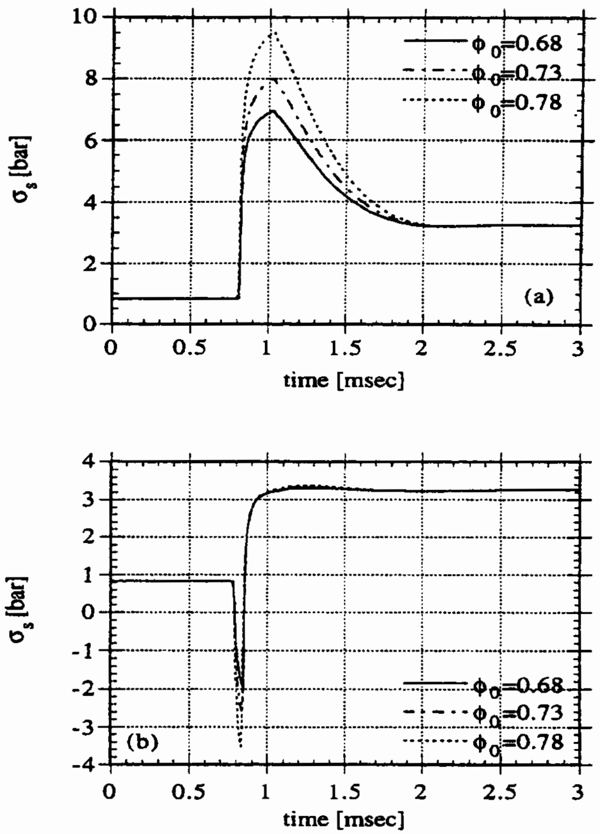

Figure 9. The influence of the initial porosity on the normal stress: (a) at the back edge of the sample and (b) at the front edge of the sample. The sample was made of SiC and it was 81 mm long. The incident shock wave Mach number was $M_i = 1.377$.

deviating from the macroscopic ones. These were assumed to be negligible in comparison to the averaged, macroscopic terms. The solution of this second-order equation, subjected to boundary and initial conditions similar to the macroscopic counterpart, will improve the conservation of the momentum balance especially for heterogeneous media and high velocities, which may produce significant variations from the average momentum flux terms.

Nondimensional analysis of the balance equations, after the onset of abrupt change in fluids' pressure and temperature, provide the theoretical basis for obtaining dominant balance equations that conform to wave equations. Four different simplified 1-D analytical solutions are then presented. The first considering post compaction wave for small porosity values, considering incompressible solid phase. The second for a compressible solid phase and a matrix of very small porosity values. Both models are compared with experimental observations of head-on collision of planar shock waves with air saturated rigid porous materials. These prove to yield good results.

The third and the fourth analytical solutions, refer to traveling weak waves in the horizontal direction. In both models, the fluid mass balance equation or its momentum balance equation conform to a pressure wave equation, with gas and matrix quantities that can be evaluated analytically. The third model refers to an isothermal case while the fourth accounts for nonisothermal conditions.

Numerical simulations of compaction waves in a 1-D saturated porous medium, are then compared with shock tube experiments. These simulations were done with and without Forchheimer terms. The case of accounting for Forchheimer terms demonstrates almost no deviation from experimental results and was by far better than the case when we did not include these terms.

References

1. Attenborough, K.: Acoustical characteristics of porous materials, *Phys. Reports* **82**(3) (1982), 179–227.
2. Bachmat, Y. and Bear, J.: Macroscopic modeling of transport phenomena in porous media: 1. The continuum approach, *Transport in Porous Media* **1** (1986), 213–240.
3. Baer, M. R.: Numerical studies of dynamic compaction of inert and energetic granular materials, *ASME J. Appl. Mech.* **55** (1988), 36–43.
4. Baer, M. R.: A numerical study of shock wave reflections on low density foam, *Shock Waves* **2** (1992), 121–124.
5. Baer, M. R. and Nunziato, J. W.: A two-phase mixture theory for the deflagration to detonation transition (DDT) in reactive granular materials, *Int. J. Multiphase Flow* **12** (1986), 861–889.
6. Bear, J. and Bachmat, Y.: *Introduction to Modeling of Transport Phenomena in Porous Media*, Kluwer Academic Publishers, Dordrecht, The Netherlands, 1990.
7. Bear, J. and Sorek, S.: Evolution of governing mass and momentum balance equations following an abrupt pressure impact in a porous medium, *Transport in Porous Media* **5** (1990), 169–185.
8. Bear, J., Sorek, S., Ben-Dor, G. and Mazor, G.: Displacement waves in saturated thermoelastic porous media: I. Basic equations, *Fluid Dynam. Res.* **9** (1992), 155–164.
9. Ben-Dor, G.: *Shock Wave Reflection Phenomena*, Springer-Verlag, New York, 1991.
10. Ben-Dor, G., Mazor, G., Igra, O., Sorek, S. and Onodera, H.: Shock wave interaction with cellular materials: II. Open cell foams; Experimental and numerical results, *Shock Waves* **3**(3) (1994), 167–179.
11. Ben-Dor, G. and Zaretsky, E. B.: Head-on interaction of planar shock waves with polyurethane foams – A semi-empirical model, *Archivem Appl. Mech.* **64** (1994), 1–8.
12. Biot, M. A.: Theory of propagation of elastic waves in fluid-saturated porous solid, *J. Acoust. Soc. Amer.* **28** (1956), 168–191.
13. Corapcioglu, M. Y.: Wave propagation in porous media – a review, In: J. Bear and M. Y. Corapcioglu (eds), *Transport Processes in Porous Media*, Kluwer Academic Publishers, Dordrecht, The Netherlands, 1991, pp. 373–469.
14. Degrande, G. and de Roeck, G.: FFT-based spectral analysis methodology for one-dimensional wave propagation in poroelastic media, *Transport in Porous Media* **9** (1992), 85–97.
15. Du Plessis, J. P. and Masliyan, J. H.: Mathematical modeling of flow through consolidated isotropic porous media, *Transport in Porous Media* **3** (1988), 145–164.
16. Du Plessis, J. P., Montillet, A., Comiti, J. and Legrand, J.: Pressure drop prediction for flow through high porosity metallic foams, *Chem. Engg. Sci.* **49**(21) (1994), 3545–3553.
17. Gelfand, B. E., Gubanov, A. V. and Timofeev, E. I.: Interaction between shock waves and porous screen, *Sov. Phys.-Fluid Mech.* **4** (1983), 79–84.

18. Gibson, L. J. and Ashby M. F.: *Cellular Solids – Structure & Properties*, Program Press, Headington Hill Hall, Oxford, England, 1988.
19. Glass, I. I. and Hall, G. J.: *Shock Tubes, Handbook of Supersonic Aerodynamics*, Sec. 18, Navond Report 1488, Vol. 6, 1959, p. 66.
20. van der Grinten, J. G. M., Smits, M. A., van der Kogel, H. and van Dongen, M. E. H.: Shock-induced wave propagation in and reflection from porous column partially saturated with water, In: H. Gronig (ed.), *Shock Tubes and Waves*, VCH Verlagsgesellschaft mbH, Weinheim, Germany, 1988, pp. 357–362.
21. Gvozdeva, L. G., Faresov, Yu. M. and Fokeev, V. P.: Interaction between air shock wave and porous compressible material, *Sov. Phys. Appl. Math. Tech. Phys.* **3** (1985), 111–115.
22. Gvozdeva, L. G. and Faresov, Yu. M.: Approximate calculation of steady state shock wave parameters in porous compressible materials, *J. Appl. Mech. Tech. Phys.* (English translation of PMTF, *Zh. Prik. Mekh. Tekh. Fiz.*), **27** (1986), 107–111.
23. Harten, A.: High resolution schemes for hyperbolic conservation laws, *J. Comput. Phys.* **49** (1983), 357–393.
24. Henderson, L. F., Virgona, R. J., Di, J. and Gvozdeva, L. G.: Refraction of a normal shock wave from nitrogen into polyurethane foam, In: Y. W. Kim (ed.), *Current Topics in Shock Waves*, American Institute of Physics, New York, U.S.A., 1990, pp. 814–818.
25. Hsu, C. T. and Cheng, P.: Thermal dispersion in a porous medium, *Int. J. Heat Mass Transfer* **33**(8) (1990), 1587–1597.
26. Igra, O. and Ben-Dor, G.: Dusty shock waves, *ASME Appl. Mech. Rev.* **41** (1988), 379–437.
27. Krylov, A., Sorek, S., Levy, A. and Ben-Dor, G.: Simple waves in saturated porous media: I. The isothermal case, *JSME Int. J. Series B* **39**(2) (1996), 294–298.
28. Landau, L. D. and Lifshitz, E. M.: *Fluid Mechanics*, 2nd edn, Pergamon Press, 1987, pp. 378–385.
29. Levy, A.: Wave Propagation in a Saturated Porous Media, PhD Thesis, Department of Mechanical Engineering, Ben-Gurion University of the Negev, Beer Sheva, Israel, 1996, (in Hebrew).
30. Levy, A., Ben-Dor, G., Skews, B. W. and Sorek, S.: Head-on collision of normal shock waves with rigid porous materials, *Experiments in Fluids* **15** (1993), 183–190.
31. Levy, A., Ben-Dor, G., Sorek, S. and Bear, J.: Jump conditions across strong compaction waves in gas saturated rigid porous media, *Shock Waves* **3**(2) (1993), 105–111.
32. Levy, A., Sorek, S., Ben-Dor, G. and Bear, J.: Evolution of the balance equations in saturated thermoelastic porous media following abrupt simultaneous changes in pressure and temperature, *Transport in Porous Media* **21** (1995), 241–268.
33. Levy, A., Sorek, S., Ben-Dor, G. and Skews B. W.: Waves propagation in saturated rigid porous media: analytical model and comparison with experimental results, *Fluid Dynam. Res.* **17** (1996), 49–65.
34. Levy A., Ben-Dor G., and Sorek, S.: Numerical investigation of the propagation of shock waves in rigid materials: development of the computer code and comparison with experimental results, *J. Fluid Mech.* **324** (1996), 163–179.
35. Li, H. and Ben-Dor, G.: Head-on interaction of weak planar shock waves with flexible porous materials – analytical model, *Int. J. Multiphase Flow* **21**(5) (1995), 941–947.
36. Li, H., Levy, A. and Ben-Dor, G.: Analytical prediction of regular reflection over porous surfaces and comparison with experiments, *J. Fluid Mech.* **282** (1995), 219–232.
37. Liepmann, H. W. and Roshko, A.: *Elements of Gas Dynamics*, Wiley, New York, U.S.A., 1957.
38. Mazor, G., Ben-Dor, G., Igra, O. and Sorek, S.: Shock wave interaction with cellular materials: Part I. Analytical investigation and governing equations, *Shock Waves* **3** (1994), 159–165.
39. Nield, D. A.: The limitations of the Brinkman–Forchheimer equation in modelling flow in a saturated porous medium and at an interface, *Int. J. Heat Fluid Flow* **12** (1991), 269–272.

40. Nield, D. A.: Modelling high speed flow of compressible fluid in a saturated porous medium, *Transport in Porous Media* **14** (1994), 85–88.
41. Nigmatulin, R. I. and Gubaidullin, A. A.: Linear waves in saturated porous media, *Transport in Porous Media* **9** (1992), 135–142.
42. Nikolaevskij, V. M.: *Mechanics of Porous and Fractured Media*, World Scientific, Singapore, 1990.
43. Olim, M., van Dongen, M. E. W., Kitamura, T. and Takayama, K.: Numerical simulation of the propagation of shock waves in compressible open-cell porous foams, *Int. J. Multiphase Flow* **20**(3) (1994), 557–568.
44. Powers, J. M., Stewart, D. S. and Krier, H.: Analysis of steady compaction waves in porous materials, *ASME J. Appl. Mech.* **56** (1989), 15–24.
45. Sandusky, H. W. and Liddiard, T. P.: *Dynamic Compaction of Porous Beds*, NSWC TR 83-256, NAVAL Surface Weapons Center, White Oak, Md., U.S.A., 1985.
46. Skews, B. W.: The reflected pressure field in the interaction of weak shock waves with a compressible porous foams, *Shock Waves* **1** (1991), 205–211.
47. Skews, B. W., Atkins, M. D. and Seitz, M. W.: The impact of shock wave on porous compressible foams, *J. Fluid Mech.* **253** (1993), 245–265.
48. Smeulders, D. M. J., de La Rosette, S. P. M. and Van Dongen, M. E. H.: Waves in partially saturated porous media, *Transport in Porous Media* **9** (1992), 25–37.
49. Sorek, S., Bear, J., Ben-Dor, G. and Mazor, G.: Shock waves in saturated thermoelastic porous media, *Transport in Porous Media* **9** (1992), 3–13.
50. Sorek, S., and Levi-Hevroni, D.: A model for solute transport following an abrupt pressure impact in nondeformable porous media, *2nd Inter. Conf. on Water Pollution Milan* 1993, pp. 77–84.
51. Sorek, S., Krylov, A., Levy, A. and Ben-Dor, G.: Simple waves in saturated porous media: II. The nonisothermal case, *JSME Int. J. Series B* **39**(2) (1996), 299–304.
52. Sorek, S.: A model for solute transport following an abrupt pressure impact in saturated porous media, *Transport in Porous Media* **22** (1996), 271–285.
53. Zaretsky, E. B. and Igra, O.: Head-on collision of a normal shock wave with a polyester foam, *The 19th Int. Symp. Shock Waves*, Marseille, France, 1993.